Article

Precise modelling of mitochondrial diseases using optimized mitoBEs

https://doi.org/10.1038/s41586-024-08469-8

Received: 24 April 2024

Accepted: 28 November 2024

Published online: 22 January 2025

Check for updates

Xiaoxue Zhang[1,2], Xue Zhang[1], Jiwu Ren[1,3], Jiayi Li[2,3], Xiaoxu Wei[2,3], Ying Yu[2], Zongyi Yi[1,2]✉ & Wensheng Wei[1,2,3]✉

The development of animal models is crucial for studying and treating mitochondrial diseases. Here we optimized adenine and cytosine deaminases to reduce off-target effects on the transcriptome and the mitochondrial genome, improving the accuracy and efficiency of our newly developed mitochondrial base editors (mitoBEs)[1]. Using these upgraded mitoBEs (version 2 (v2)), we targeted 70 mouse mitochondrial DNA mutations analogous to human pathogenic variants[2], establishing a foundation for mitochondrial disease mouse models. Circular RNA-encoded mitoBEs v2 achieved up to 82% editing efficiency in mice without detectable off-target effects in the nuclear genome. The edited mitochondrial DNA persisted across various tissues and was maternally inherited, resulting in F_1 generation mice with mutation loads as high as 100% and some mice exhibiting editing only at the target site. By optimizing the transcription activator-like effector (TALE) binding site, we developed a single-base-editing mouse model for the *mt-Nd5* A12784G mutation. Phenotypic evaluations led to the creation of mouse models for the *mt-Atp6* T8591C and *mt-Nd5* A12784G mutations, exhibiting phenotypes corresponding to the reduced heart rate seen in Leigh syndrome and the vision loss characteristic of Leber's hereditary optic neuropathy, respectively. Moreover, the *mt-Atp6* T8591C mutation proved to be more deleterious than *mt-Nd5* A12784G, affecting embryonic development and rapidly diminishing through successive generations. These upgraded mitoBEs offer a highly efficient and precise strategy for constructing mitochondrial disease models, laying a foundation for further research in this field.

Mitochondrial DNA (mtDNA) typically exists in multiple copies, comprising approximately 16-kilobase circular double-stranded DNA molecules in both human and mouse cells, encoding 13 proteins involved in oxidative phosphorylation, 22 transfer RNAs (tRNAs) and 2 ribosomal RNAs (rRNAs)[3]. Mutations in mtDNA can be either homoplasmic, affecting all copies of the mtDNA, or heteroplasmic, for which mutant and wild-type mtDNAs coexist. Such mutations disrupt mitochondrial function and occur in about 1 in 5,000 individuals[4,5]. Among the most well-known diseases associated with mitochondrial mutations are Leigh syndrome[6] and Leber's hereditary optic neuropathy (LHON)[7]. Leigh syndrome symptoms include developmental delay, hypotonia, motor and respiratory issues, eye movement disorders, facial dysmorphism, seizures and ataxia[8]. LHON causes vision loss, central scotoma, optic atrophy, nystagmus and colour vision abnormalities[9]. These mitochondrial diseases typically appear in infancy[10] or adulthood[11], affecting critical organs such as the heart, eyes, ears and nervous system[12]. The scarcity of suitable animal models has hindered research and treatment[13,14], making their development crucial for progress.

Mouse models for mitochondrial diseases were historically generated through chemical induction and genetic engineering[14,15]. However, these approaches lacked precise control over mutations and were complex and costly. Few models were successfully produced[14]. Gene-editing tools such as transcription activator-like effector (TALE) nucleases (TALENs)[16] and zinc-finger nucleases (ZFNs)[17] targeting mitochondria enabled more direct manipulation of mtDNA, but precise base changes remained challenging. Recently, various laboratories have developed mitochondrial base-editing tools capable of performing C-to-T and A-to-G edits on mtDNA, such as DddA-derived cytosine base editors (DdCBEs)[18] and TALE-linked deaminases (TALEDs)[19] that use the double-stranded DNA deaminase DddA protein. Our laboratory recently developed mitoBEs[1,20], a tool that integrates a nickase with a single-stranded DNA deaminase to achieve C-to-T and A-to-G base editing in mtDNA. Compared to DdCBEs and TALEDs, mitoBEs have demonstrated high efficiency and strand specificity, with minimal off-target effects in both mitochondrial and nuclear genomes[1]. Consequently, mitoBEs are particularly suitable for creating precise animal models of mitochondrial diseases.

So far, 97 disease-associated mitochondrial mutations have been identified, with 92 being point mutations[2]. Of these, 85 point mutations are amenable to modelling with mitoBEs, allowing for precise editing

[1]Changping Laboratory, Beijing, The People's Republic of China. [2]Biomedical Pioneering Innovation Center, Peking University Genome Editing Research Center, State Key Laboratory of Gene Function and Modulation Research, School of Life Sciences, Peking University, Beijing, The People's Republic of China. [3]Peking-Tsinghua Center for Life Sciences, Academy for Advanced Interdisciplinary Studies, Peking University, Beijing, The People's Republic of China. ✉e-mail: zongyiyi@pku.edu.cn; wswei@pku.edu.cn

and potential therapeutic approaches. Here, to precisely correlate disease phenotypes to genotypes, we further improved the precision of mitoBEs to facilitate the development of animal models for mitochondrial diseases.

Off-target effect of original mitoBEs

To establish a direct link between mutations and disease phenotypes when creating disease models with base-editing tools, it is essential to eliminate off-target effects. For effective mitochondrial disease modelling using mitoBEs, RNA-encoded mitoBEs must be injected into mouse zygotes. Previous studies with plasmid transfection found no notable off-target sites of mitoBEs in the mitochondrial or nuclear genomes[1]. However, a comprehensive evaluation of off-target effects in RNA-encoded mitoBE systems is necessary.

We conducted a systematic analysis of off-target effects induced by RNA-encoded mitoBEs at the whole-genome and whole-transcriptome levels. We designed a mitochondrial adenine base editor (mitoABE; left TALE-fused TadA8e-V106W (a variant of the TadA protein) and right TALE-fused MutH) and a mitochondrial cytosine base editor (mitoCBE; left TALE-fused APOBEC1 and uracil glycosylase inhibitor (UGI) and right TALE-fused MutH), both targeting the *MT-RNR2* gene, synthesized as mRNA and transfected into HEK293T cells. mitoABE achieved approximately 70% editing efficiency with minimal off-target effects in the mitochondrial genome at a sequencing depth of about 26,000× (Extended Data Fig. 1a,b), but induced widespread A-to-G off-target editing at the transcriptome level compared to the enhanced green fluorescent protein (eGFP) control (Extended Data Fig. 1c). mitoCBE also reached about 70% editing efficiency but exhibited some C-to-T off-target effects in the mitochondrial genome, particularly at position 5746 with an efficiency of about 18% (Extended Data Fig. 1d,e). Plasmid-encoded mitoABE and mitoCBE achieved 14% and 26% editing efficiency, respectively (Extended Data Fig. 2a), indicating that mRNA-encoded mitoBEs have much higher editing efficiencies, making off-target issues more evident. Examination of the 200-base-pair (bp) regions upstream and downstream of all off-target sites revealed no potential TALE-binding sites with 0 or 1 mismatch (Supplementary Table 1), indicating that these off-target effects are independent of TALEs. Analysis of the 5-bp sequences flanking the off-target sites revealed a 5′-TC motif (Extended Data Fig. 2b), consistent with the sequence preference of APOBEC1 (refs. 21,22), suggesting that the off-target effects from mitoCBE are probably due to random deamination by APOBEC1. Unlike mitoABE, mitoCBE did not induce off-target editing at the transcriptome level (Extended Data Fig. 1f).

Precision optimization of mitoBEs

To enhance mitoBEs for disease model applications, we improved the deaminases used, increasing their precision and efficiency. For mitoABEs, minimizing off-target effects on the transcriptome is crucial. Whereas various cytosine deaminases are used in cytosine base editing, only TadA mutants have been successfully used for adenine base editing. Utilizing AlphaFold2 (ref. 23), we predicted the structure of TadA8e-V106W and analysed its RNA interactions by comparing it with *Staphylococcus aureus* TadA (ref. 24). We identified six amino acids (Arg21, Glu27, Val28, Val82, Trp106 and Arg107) potentially interacting with RNA and conducted saturation mutagenesis (Fig. 1a). Screening through plasmid transfection at the *MT-RNR2* target site yielded 28 TadA8e-V106W variants with editing efficiencies equal to or better than that of the original enzyme (Fig. 1b). Notably, the alterations Val-28Phe (V28F), Val28Met (V28M) and Val28Tyr (V28Y) enhanced the targeted editing efficiency of TadA8e-V106W (Fig. 1b). We also assessed the off-target effects of these variants on six RNA sites commonly used to assess TadA mutants' off-target impacts[25]. The V28F alteration improved on-target editing efficiency and markedly reduced RNA off-target effects, achieving a 52-fold higher editing efficiency at the DNA target compared to the average RNA off-target sites (Fig. 1c). We then applied TadA8e-V106W-V28F to mitochondrial adenine base editing, naming it mitoABE v2. At the *MT-RNR2* site, mitoABE v2 achieved an efficiency of 26%, nearly doubling the 14% efficiency of the original mitoABE (Fig. 1b). At some sites, the editing efficiency of mitoABE v2 was higher than that of mitoABE (Extended Data Fig. 3a). Moreover, transcriptome-level off-target effects of mitoABE v2 were reduced compared to those of mitoABE, aligning closely with those in the eGFP control group (Fig. 1d). In essence, mitoABE v2 induces a basal level of RNA off-target mutations.

For mitoCBEs, we tested 16 cytosine deaminases fused with UGI at the *MT-RNR2* site in HEK293T cells using mRNA-encoded mitoCBEs. The tested deaminases included AID (ref. 26), evoAPOBEC1 (ref. 27), evoCDA1 (ref. 27), hA3A (refs. 28,29), evoFERNY (ref. 27) and 11 TadA-derived cytosine deaminases, including CBE6a, CBE6b, CBE6c, CBE6d, TadA-CDa, TadA-CDb, TadA-CDc, TadA-CDd, eTD-CBE, eTD-CBEa and eTD-CBEm (refs. 30–32). Our results indicated that substituting APOBEC1 with other deaminases such as evoAPOBEC1, evoCDA1, hA3A, evoFERNY and some TadA-derived deaminases led to efficient editing, with CBE6d achieving the highest editing efficiency of 60% (Fig. 1e). We also observed that TadA-derived cytosine deaminases provided a narrower editing window, reducing bystander off-target effects (Fig. 1e). Further analysis of mitochondrial genome off-target effects revealed that TadA-derived cytidine deaminases offered better precision than APOBEC1, evoAPOBEC1, evoCDA1, hA3A and evoFERNY, with C-to-T mutation levels comparable to those seen in the untreated group (Fig. 1f). In summary, CBE6d shows higher editing efficiency, a narrower editing window and minimal mtDNA off-target effects compared to APOBEC1. Additionally, the TALE-fused APOBEC1 and UGI vector was challenging to construct and exhibited strong bacterial toxicity, whereas TALE-fused CBE6d and UGI vector did not, making mitoCBEs easier to use. Consequently, we selected CBE6d as the preferred cytosine deaminase for future mitoCBE applications, naming the tool using CBE6d protein as mitoCBE v2. Both mitoABE v2 and mitoCBE v2 are collectively referred to as upgraded mitoBEs, mitoBEs v2. The editing efficiency of mitoCBE v2 was higher than that of mitoCBE at some sites (Extended Data Fig. 3b).

Whole-genome sequencing showed no obvious off-target sites in the nuclear genome for original and upgraded mitoBEs at above 75× sequencing depth (Extended Data Fig. 2c–f). Further comprehensive off-target assessments revealed no significant differential sites between any editing tools and their controls (all P values > 0.05) and demonstrated exceptionally high concordance of variant sites between experimental and control groups (r > 0.98; Extended Data Fig. 2g–l). We also used TALENoffer[33] to predict nuclear genome off-target sites, and found that neither mitoBEs nor mitoBEs v2 produced editing at the top 500 potential target sites (Supplementary Tables 2 and 3). These multi-faceted off-target analyses collectively indicate that mitoBEs show high nuclear genome safety.

Creating pathogenic mutation in Neuro-2a

By aligning human pathogenic 85 mtDNA point mutations with the mouse mitochondrial genome, we identified 70 editable sites, which include 36 mutations in tRNA genes, 33 in protein-coding genes and 1 in an rRNA gene (Fig. 2a and Supplementary Table 4). Notably, the T7928C mutation is located in the overlapping region of the *mt-Atp6* and *mt-Atp8* genes. The remaining 14 sites harbour bases identical to the pathogenic human equivalents, excluding them as potential mouse mitochondrial pathogenic sites (Supplementary Table 4).

We designed mitoBEs v2 to target these 70 sites by placing the target site (A or C) at the centre of the editing window. We selected 20-bp sequences on both sides, 8 bp away from the target site, to serve as the binding sequences for the TALEs. On the basis of our previous experience, we use Nt.BspD6I(C), which typically nicks the DNA strand

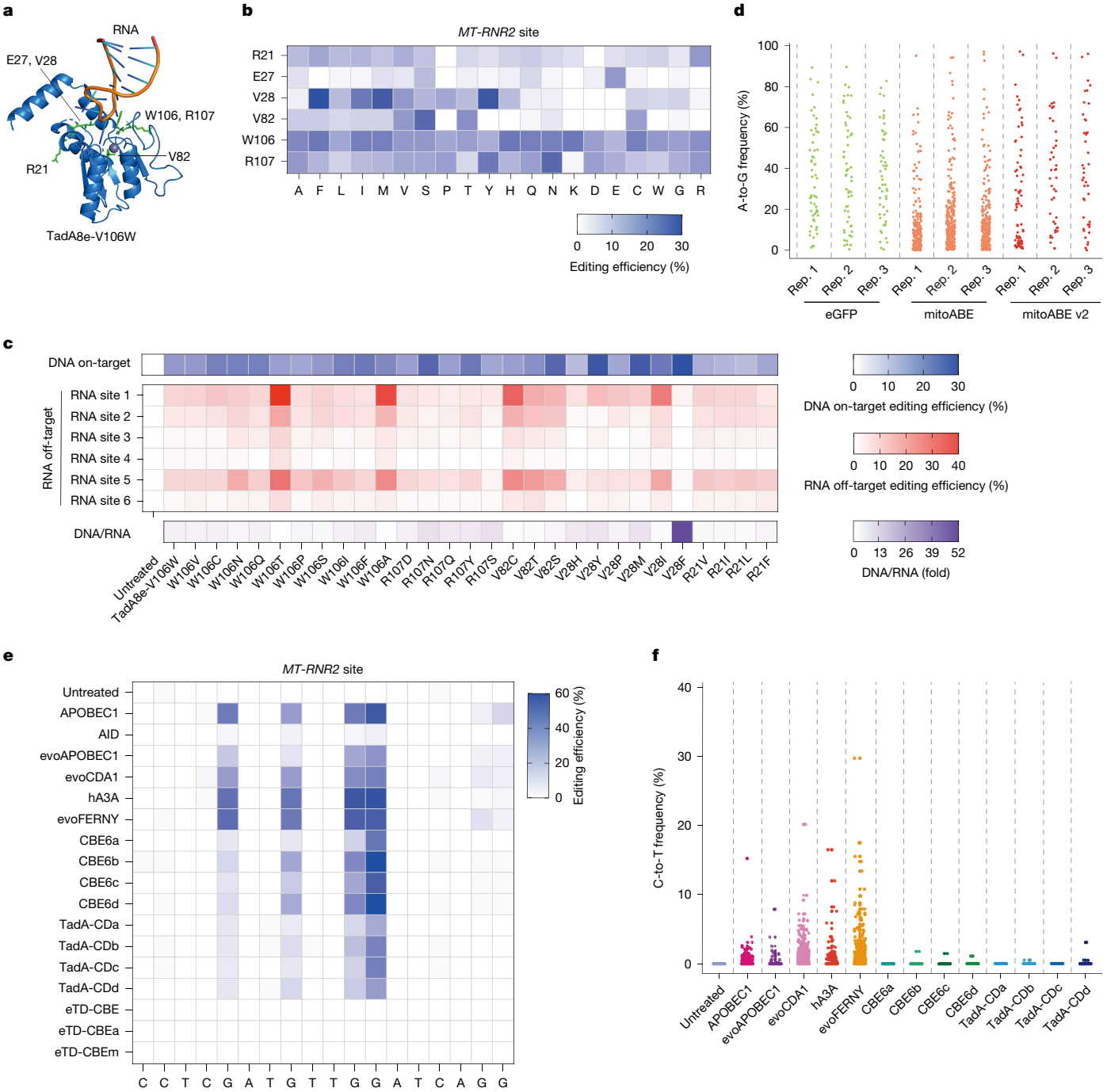

Fig. 1 | Precision optimization of mitoBEs. a, Predicted structure of TadA8e-V106W interacting with RNA, modelled using AlphaFold2. The amino acids selected for saturation mutagenesis are marked in green. Note that amino acids have been written using the single-letter code. **b**, Editing efficiency of TadA8e-V106W mutants at the *MT-RNR2* site, detected 3 days after plasmid transfection into HEK293T cells. **c**, Editing efficiency of 28 TadA8e-V106W mutants at the DNA on-target site (top), and 6 RNA off-target sites (middle), and the ratio of DNA on-target editing efficiency to RNA off-target editing efficiency (bottom), detected 3 days after plasmid transfection into HEK293T cells. **d**, Transcriptome off-target effects of mRNA-encoded eGFP, *MT-RNR2*-targeting mitoABE, and mitoABE v2. Rep., replicate. **e**, Editing efficiency of mRNA-encoded *MT-RNR2*-targeting mitoCBEs using different cytosine deaminases in HEK293T cells. For **b**, **c** and **e**, data are presented as mean from $n = 3$ independent biological replicates. **f**, mtDNA off-target effects of mRNA-encoded mitoCBEs using different cytosine deaminases. All data were obtained from three biological replicates with consistent results.

recognized by the fused TALE, to effectively edit the target site on the opposite strand (Fig. 2b).

To address the low efficiency of plasmid transfection in mouse cells, we engineered mitoBEs v2 into a circular RNA (circRNA) vector. This circRNA was synthesized in vitro using a previously developed method[34,35] and transfected into Neuro-2a cells. At 3 days post-transfection, cells were collected to assess the editing efficiency (Fig. 2c). Initial screening indicated successful editing at 68 of 70 targeted sites across rRNA, tRNA and protein-coding genes (Fig. 2d and Extended Data Fig. 4). High editing efficiencies were observed at sites including *mt-Rnr1* A978G, *mt-TrnV* G1029A, *mt-TrnK* G7741A, *mt-TrnK* G7763A, *mt-Atp6* T8576C, *mt-Atp6* T8591C, *mt-Nd5* T12499C and *mt-Nd5* A12784G, averaging around 20% (Fig. 2d and Extended Data Fig. 4). The other 60 sites exhibited lower editing efficiencies, averaging below 10% (Extended Data Fig. 4). These

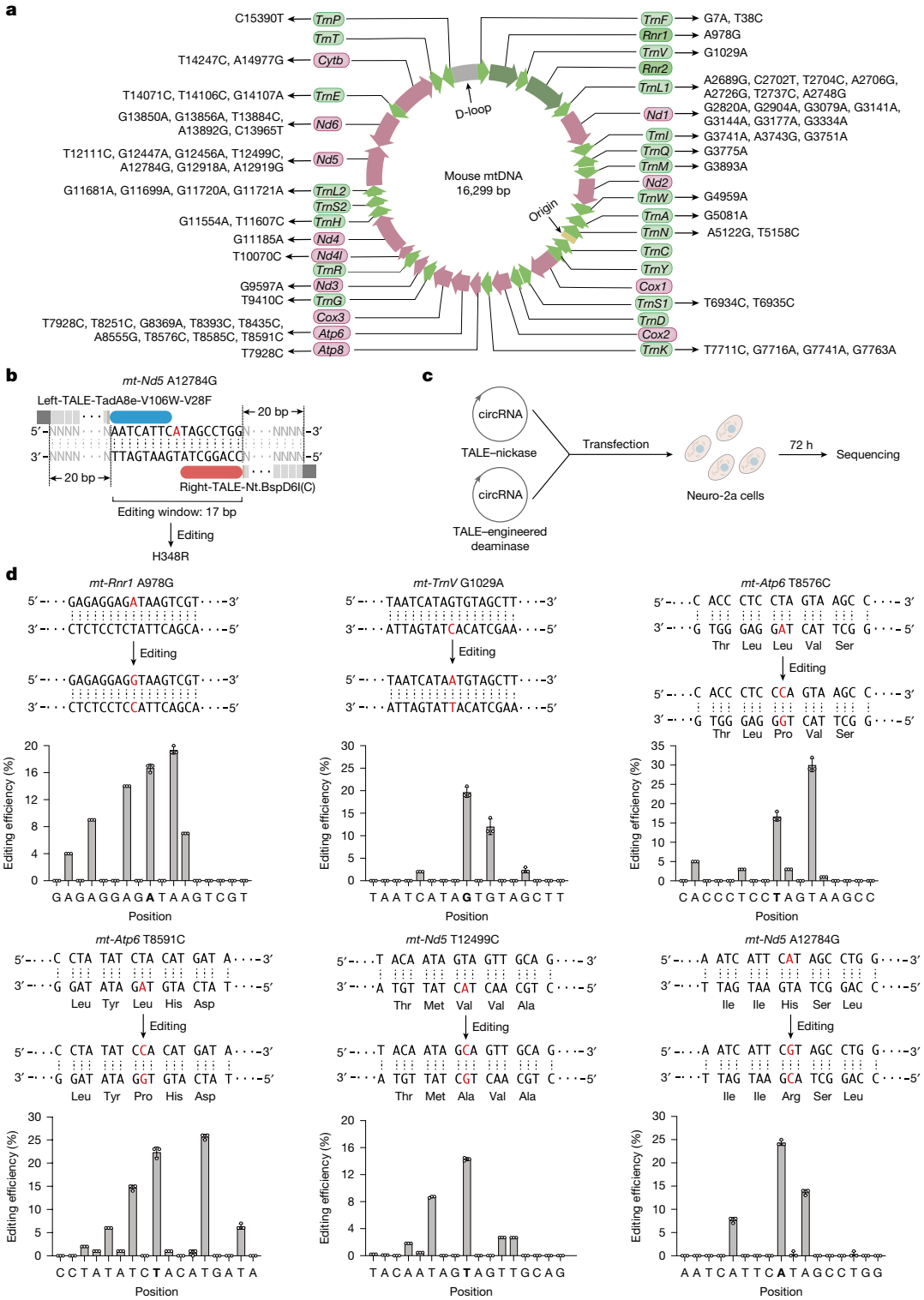

Fig. 2 | Screening homologous pathogenic sites efficiently edited by mitoBEs v2 in Neuro-2a cells. a, Distribution of 70 homologous pathogenic mutations in mouse mitochondrial genes. Dark green represents rRNA genes, light green represents tRNA genes, and red represents protein-coding genes. The T7928C mutation is located in both the *mt-Atp6* and *mt-Atp8* loci. **b**, Schematic representation of the design of mitoBEs v2 to generate disease-causing point mutations. Using *mt-Nd5* A12784G as an example, the target editing site (A; in red) is placed at the centre of the editing window, and 20-bp sequences on either side, positioned 8 bp away from the target site, are selected for TALE recognition and binding. The TALE fused with the deaminase TadA8e-V106W-V28F is designed to recognize the strand containing the target editing site, and the TALE fused with the nickase Nt.BspD6I(C) is designed to recognize the opposite strand. Achieving A-to-G editing at position 12784 of *mt-Nd5* mutates the 348th amino acid of the NU5M protein from histidine to arginine (H348R). **c**, Schematic diagram of transfection of circRNA-encoded mitoBEs v2 into Neuro-2a cells. At 3 days post-transfection, cells were collected to detect target site editing efficiency. Schematic reproduced from ref. 1, Springer Nature Limited. **d**, Editing efficiency of mitoBEs v2 at multiple mouse sites, including *mt-Rnr1* A978G, *mt-TrnV* G1029A, *mt-Atp6* T8576C, *mt-Atp6* T8591C, *mt-Nd5* T12499C and *mt-Nd5* A12784G. The red base indicates the target base and its edited result. The horizontal axis shows 17 bases within the editing window, with the bold base in the middle representing the target site. The vertical axis represents the editing efficiency. Data are presented as mean ± s.d. from $n = 3$ independent biological replicates.

results demonstrate that mitoBEs v2 can effectively achieve A-to-G and C-to-T mitochondrial base editing in mouse cells, demonstrating high editing efficiency and strong strand-selectivity minimizing off-target effects on the opposite strand.

mitoBEs v2 achieve editing in mice

We identified two sites with the highest editing efficiency in Neuro-2a cells, *mt-Atp6* T8591C and *mt-Nd5* A12784G, as starting points for developing mouse models. Editing efficiencies at these sites were 23% and 25%, respectively. In mice, the *mt-Atp6* T8591C mutation corresponds to the human m.T9191C mutation, resulting in a p.Leu222Pro substitution in the ATP6 protein, which is linked to Leigh syndrome[36]. The *mt-Nd5* A12784G mutation corresponds to the human m.A13379G mutation, leading to a p.His348Arg change in the NU5M protein, associated with LHON disease[37].

We synthesized mRNA and circRNA targeting the *mt-Atp6* T8591C and *mt-Nd5* A12784G sites and microinjected them into C57BL/6J mouse embryos at the one-cell stage. Embryos were collected for editing efficiency assessment at the blastocyst stage, approximately 3 days post-microinjection (Fig. 3a). Groups of five embryos each were sampled for testing. For both mRNA and circRNA targeting each site, we attempted injections at three concentrations: 75, 150 and 300 ng μl^{-1}. Both forms of RNA showed a higher editing efficiency at 150 ng μl^{-1} (Fig. 3b,c), with circRNA-encoded mitoBEs v2 exhibiting superior efficiency over mRNA, achieving efficiencies of 65% for *mt-Atp6* T8591C and 62% for *mt-Nd5* A12784G (Fig. 3b,c). This enhanced performance is probably due to the greater stability of circRNA, allowing for more sustained protein expression[34,35]. Moreover, editing efficiency in mouse embryos using circRNA-encoded mitoBEs v2 was much higher than in Neuro-2a cells (Figs. 2d and 3b,c), probably owing to the inherently low transfection efficiency of Neuro-2a cells and the higher quantity of RNA delivered through microinjection compared to liposome transfection.

We microinjected one-cell-stage mouse embryos with circRNA-encoded mitoBEs and mitoBEs v2 at a concentration of 150 ng μl^{-1} and transplanted these embryos into surrogate mother mice. About a week after birth, we evaluated editing efficiency by sampling toes from the F_0 generation mice (Fig. 3d). Compared to the original mitoABE, mitoABE v2 targeting *mt-Atp6* T8591C and *mt-Nd5* A12784G sites showed significantly higher editing efficiencies (Fig. 3e,f). The average editing efficiency of mitoABE v2 in F_0 mice was 46% for *mt-Atp6* T8591C and 44% for *mt-Nd5* A12784G, with maximum efficiencies of 68% and 82%, respectively. By contrast, mitoABE had average efficiencies of 30% and 38%, with maximum efficiencies of 50% and 55% (Fig. 3e,f). Examination of the editing results within the editing window for F_0 mice (No. 1, No. 2 and No. 3, numbered according to their appearance in the study) revealed that the target sites were at or near the highest editing positions within their respective windows, showing strong strand selectivity (Extended Data Fig. 5a,b).

The *mt-Atp6* T8591C site had six mutations within the editing window; thus, we named these mice *mt-Atp6* T8591C(6*). The six mutations occurred at positions 8585, 8587, 8589, 8591, 8595 and 8598, with T8589C, T8595C and T8598C being synonymous. The amino acid changes caused by the mutations T8585C, T8587C and T8591C were Leu220Pro, Tyr221His and Leu222Pro, with lower editing efficiencies at sites 8585 and 8587 compared to 8591 (Extended Data Fig. 5a). For the *mt-Nd5* A12784G site, there were three mutations within the editing window, so we named these mice *mt-Nd5* A12784G(3*), corresponding to mutations at 12780, 12784 and 12786. These resulted in Ile347Val, His348Arg and Ser349Gly, with site 12874 showing the highest editing efficiency (Extended Data Fig. 5b). In the three *mt-Atp6* T8591C(6*) F_0 mice, the proportion of reads edited only at the target site were 5.56%, 5.2% and 6.35% of all edited reads (Extended Data Fig. 5c), whereas in *mt-Nd5* A12784G(3*) F_0 mice, the percentages were 11.94%, 25.6% and 23.56% (Extended Data Fig. 5d).

Additionally, the editing efficiency of circRNA-encoded mitoBEs v2 was higher than that of mRNA-encoded versions for F_0 mice (Extended Data Fig. 6a,b). Control mice injected with buffer had a birth rate close to 30%. In comparison, the birth rates of *mt-Atp6* T8591C(6*) and *mt-Nd5* A12784G(3*) F_0 mice were approximately 10% and 30%, respectively (Fig. 3g). The significantly lower birth rate for *mt-Atp6* T8591C(6*) F_0 mice suggests that these mutations were harmful to embryonic development, whereas *mt-Nd5* A12784G(3*) mutations had no such effect, despite both sites having comparable editing efficiencies (Fig. 3e,f).

mitoBEs v2 can be widely applied to establish various mitochondrial disease models, including *mt-Rnr1* A978G, *mt-TrnV* G1029A, *mt-TrnK* G7741A, *mt-Atp6* T8251C, *mt-Atp6* T8576C and *mt-Nd5* T12499C. In F_0 mice, these sites achieved maximum editing efficiencies of 39%, 66%, 20%, 20%, 70% and 45%, respectively (Fig. 3h,i and Extended Data Fig. 6c–f). Notably, for cytosine base editing at *mt-TrnV* G1029A and *mt-TrnK* G7741A, mitoCBE using APOBEC1 failed to edit F_0 mice, but CBE6d succeeded, with up to 66% efficiency at the targeted site (Fig. 3h,i). Of the 200 embryos at sites 1029 and 7741 using mitoCBE and mitoCBE v2, 6 and 16 mice were born from mitoCBE, none with edits, whereas mitoCBE v2 produced 30 and 70 mice, respectively, most with edits (Fig. 3h,i). This suggests that the mitochondrion-targeted TALE-fused APOBEC1 and UGI protein may be toxic to embryos, and further studies are needed.

F_0 mice generally had adjacent edits within the editing window. The *mt-Rnr1* A978G, *mt-TrnV* G1029A, *mt-TrnK* G7741A, *mt-Atp6* T8251C, *mt-Atp6* T8576C and *mt-Nd5* T12499C sites contain 3, 3, 2, 4, 2 and 4 editing sites, respectively. Mice were thus named *mt-Rnr1* A978G(3*), *mt-TrnV* G1029A(3*), *mt-TrnK* G7741A(2*), *mt-Atp6* T8251C(4*), *mt-Atp6* T8576C(2*) and *mt-Nd5* T12499C(4*) (Extended Data Fig. 6g–l). Excluding synonymous mutations, the *mt-Atp6* T8251C(4*), *mt-Atp6* T8576C(2*) and *mt-Nd5* T12499C(4*) models include 1, 2 and 3 amino acids changes, respectively (Extended Data Fig. 6j–l). The establishment of these models offers valuable opportunities to study the relationship between mtDNA mutations and mitochondrial disease phenotypes.

Creating clean genetic background models

We evaluated the editing precision of mitoBEs v2 in F_0 mice by analysing the mitochondrial and nuclear genomes at the *mt-Atp6* T8591C and *mt-Nd5* A12784G sites. No obvious off-target sites were detected in the mitochondrial genome at above 2,800× depth (Fig. 3j,k and Extended Data Fig. 7a–c). For the nuclear genome at about 56× sequencing depth, we did not detect any notable off-target sites in the two mouse models (Fig. 3l,m). TALENoffer analysis also revealed no TALE-related off-target hits (Supplementary Table 5), indicating that these mouse models maintain a clean genetic background. Multilevel analyses revealed no notable nuclear off-targets in multiple mouse models (Extended Data Fig. 7d–i). This shows that mitoBEs v2 can establish mitochondrial disease models with a very clean genetic background.

Widespread and enduring editing in mice

To investigate the longevity and distribution of mtDNA edits using mitoBEs v2, we measured editing efficiency in 26 different tissues from two 2-month-old F_0 mice. For *mt-Atp6* T8591C, editing efficiencies in the toes of F_0 mice No. 4 and No. 5 were about 40% at 1 week post-birth (Fig. 4a) and remained stable across tissues, with some exceeding 60% (Fig. 4b). For *mt-Nd5* A12784G, toe editing efficiencies were approximately 60% at 1 week after birth (Fig. 4c), with F_0 No. 4 showing around 40% efficiency in most tissues at 2 months post-birth and F_0 No. 5 maintained 60% across tissues (Fig. 4d).

We also genotyped various tissues from two 6-month-old F_0 mice. At 6 months post-birth, the editing levels across tissues were similar to those observed in toe samples taken 1 week post-birth, with some fluctuations in a few tissues such as the caecum and femur of *mt-Atp6* T8591C(6*) F_0

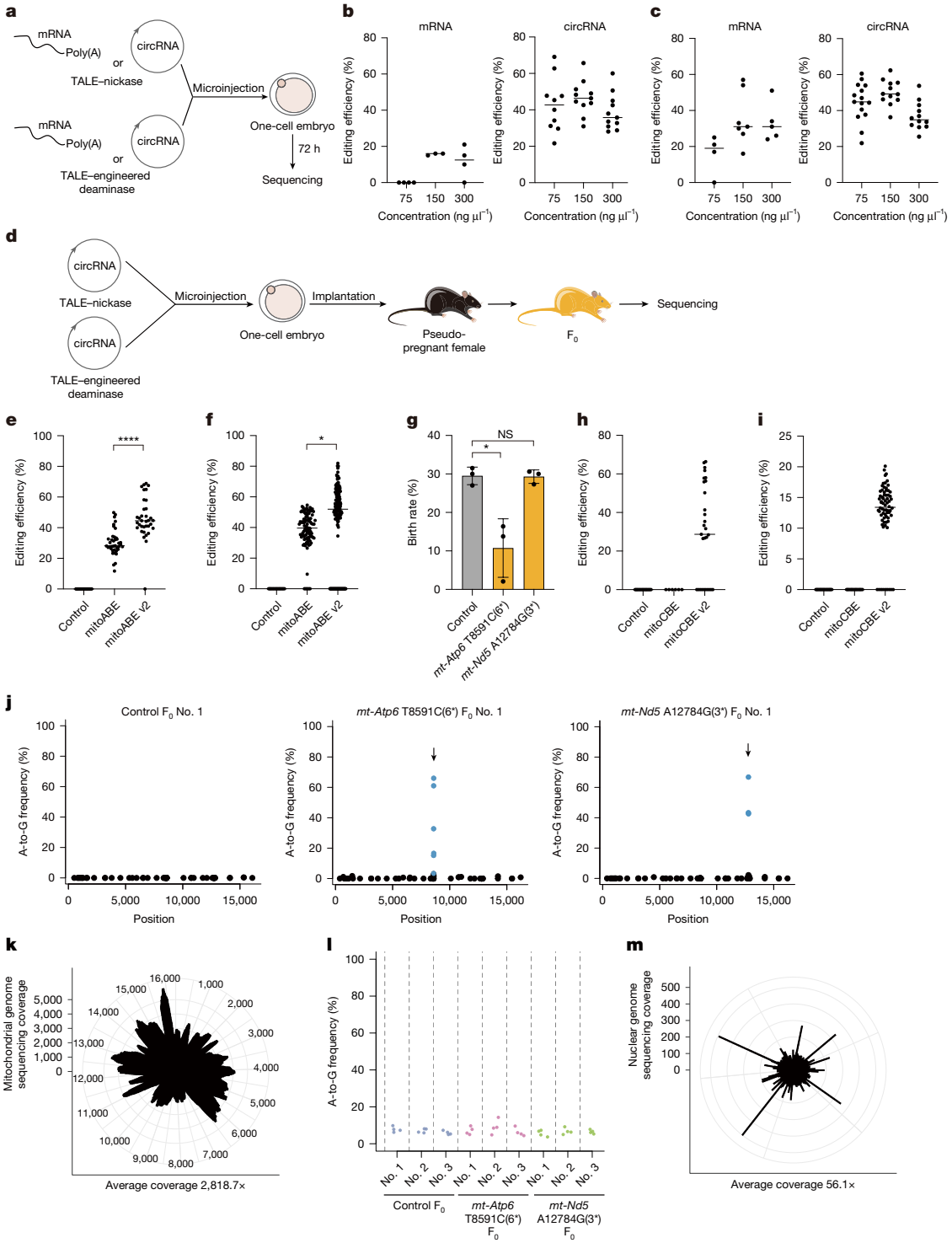

Fig. 3 | Establishing mitochondrial disease mouse models with clean genetic background using mitoBEs v2. a, Schematic diagram showing the microinjection of mRNA-encoded and circRNA-encoded mitoBEs v2 into mouse embryos and editing efficiency detection. **b**,**c**, Mouse embryo editing efficiency of *mt-Atp6* T8591C (**b**) and *mt-Nd5* A12784G (**c**). Sample size $n = 4$, 3 and 4 for mRNA and $n = 10$, 11 and 11 for circRNA (**b**), $n = 4$, 7 and 5 for mRNA and $n = 15$, 12 and 12 for circRNA (**c**); centre lines, medians. **d**, Schematic diagram depicting the microinjection of circRNA-encoded mitoBEs v2 into mouse embryos and transplantation. Schematic reproduced from ref. 35, CC BY 4.0 (https://creativecommons.org/licenses/by/4.0/). **e**,**f**, F_0 mouse editing efficiency at *mt-Atp6* T8591C (**e**) and *mt-Nd5* A12784G (**f**). Number of F_0 mice $n = 18$, 39 and 35 (**e**) and $n = 18$, 95 and 151 (**f**); centre lines, medians. **g**, Birth rates of control, *mt-Atp6* T8591C(6*) and *mt-Nd5* A12784G(3*) F_0 mice. Data are presented as mean ± s.d. from $n = 3$ independent biological replicates. For **e**–**g**, a two-tailed Student's *t*-test was used for statistical analysis. $^{****}P < 0.0001$ (**e**); $^{*}P = 0.0386$ (**f**); $^{*}P = 0.015$ and $^{NS}P = 0.915$ (>0.05, not significant (NS); **g**). **h**,**i**, F_0 mouse editing efficiency at *mt-TrnV* G1029A (**h**) and *mt-TrnK* G7741A (**i**); centre lines, medians. Number of F_0 mice $n = 18$, 6 and 29 (**h**) and $n = 18$, 16 and 70 (**i**). **j**, Average A-to-G mutation frequency on the mitochondrial genome for control (left), *mt-Atp6* T8591C(6*) (middle) and *mt-Nd5* A12784G(3*) (right) F_0 No. 1 mice. The blue circles (indicated by arrows) represent the mutation frequency of adenines within the editing window, and the black circles represent the mutation frequency of other adenines in the mitochondrial genome. **k**, Average mitochondrial genome sequencing coverage for control, *mt-Atp6* T8591C(6*) and *mt-Nd5* A12784G(3*) (No. 1, No. 2 and No. 3) F_0 mice. **l**, Average A-to-G off-target mutation frequency on the nuclear genome for the mice in **k**. **m**, Average nuclear genome sequencing coverage for the mice in **k**.

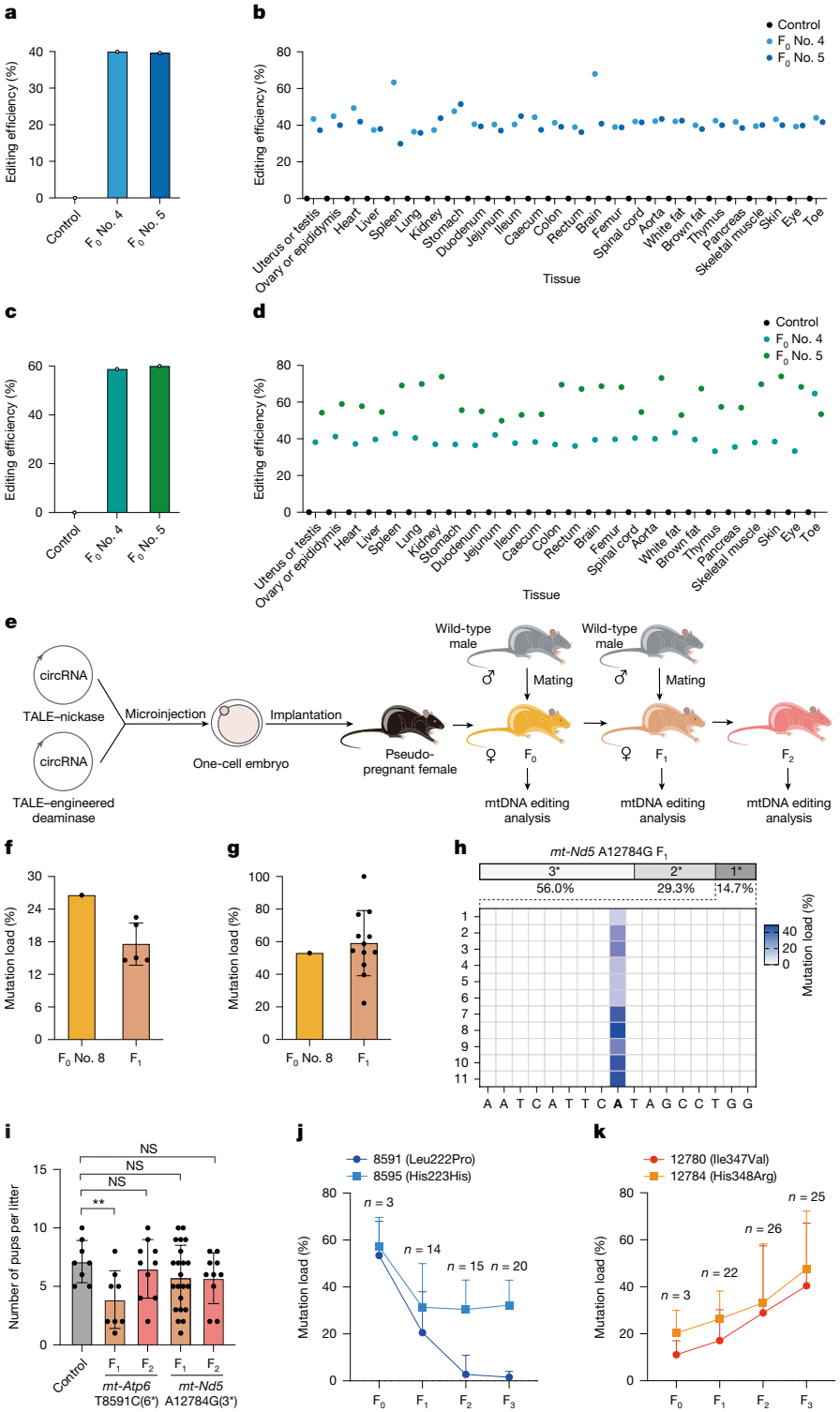

Fig. 4 | Mitochondrial editing results are tissue-wide, durable and inheritable. a, Toe tissue editing efficiency of control and *mt-Atp6* T8591C(6*) F_0 mice (No. 4 and No. 5) at 1 week after birth. **b**, Editing efficiency in 26 different tissues from mice in **a** at 2 months after birth. **c**, Toe tissue editing efficiency of control and *mt-Nd5* A12784G(3*) F_0 mice (No. 4 and No. 5) at 1 week after birth. **d**, Editing efficiency in 26 different tissues from mice in **c** at 2 months after birth. **e**, Illustration of mating edited female mice with wild-type male mice to generate offspring. Schematic reproduced from ref. 35, CC BY 4.0 (https://creativecommons.org/licenses/by/4.0/). **f**, Target site mutation load in F_1 mice generated from the *mt-Atp6* T8591C(6*) F_0 No. 8 mouse. **g**, Target site mutation load in F_1 mice generated from the *mt-Nd5* A12784G(3*) F_0 No. 8 mouse. For **f** and **g**, number of F_1 mice $n = 5$ (**f**) and 12 (**g**). **h**, Mutation status of F_1 mice generated from *mt-Nd5* A12784G(3*) F_0 mice and mutation load of *mt-Nd5* A12784G F_1 mice with single mutation. 3* indicates that the site contains three mutations (A12780G, A12784G and A12786G); 2* indicates that the site contains two mutations (A12780G and A12784G or A12784G and A12786G); 1* indicates that the site contains a single mutation (A12784G). Horizontal axis shows editing window and bold base indicating the target site 12784. **i**, Number of F_1 and F_2 mice per litter born from control, *mt-Atp6* T8591C(6*) and *mt-Nd5* A12784G(3*) mice; number of litters $n = 8, 8, 10, 22$ and 10. Statistical analysis was performed using a two-tailed Student's *t*-test. The *P* values for *mt-Atp6* T8591C(6*) F_1, *mt-Atp6* T8591C(6*) F_2, *mt-Nd5* A12784G(3*) F_1 and *mt-Nd5* A12784G(3*) F_2 versus the control, respectively, were 0.0096 (**), 0.5624 (>0.05, NS), 0.2079 (>0.05, NS) and 0.1555 (>0.05, NS). **j**,**k**, Mutation inheritance of *mt-Atp6* T8591C(6*) (**j**) and *mt-Nd5* A12784G(3*) (**k**) mice. Data are presented as mean ± s.d. from $n \geq 3$ independent biological replicates.

No. 6 and the brown fat of *mt-Atp6* T8591C(6*) F_0 No. 7 (Extended Data Fig. 8a–d). These variations may be due to the tissue-specific mtDNA genetic bottleneck influenced by environmental factors[38]. These results demonstrate that the mtDNA edits induced by mitoBEs v2 are present and persistent in multiple tissues, although efficiency may vary.

Inheritability of editing in mice

We investigated the inheritability of mtDNA edits by breeding female mice with edited mtDNA with wild-type male mice (Fig. 4e). In F_1 mice, mutation loads at target sites varied. For F_1 mice descended from the *mt-Atp6* T8591C F_0 No. 8 mouse, which had an editing efficiency of 27%, the average mutation load was around 18%, ranging from 14% to 22%. The mutation load in F_1 mice was lower than that of the F_0 No. 8 mouse (Fig. 4f). Three litters of F_1 mice derived from the *mt-Nd5* A12784G(3*) F_0 No. 8 mouse, which had a target site editing efficiency of 53%, produced eight mutant mice exhibiting 100% target site mutation loads. The average mutation loads in these three litters of F_1 mice were higher than that of the F_0 No. 8 mouse (Fig. 4g and Extended Data Fig. 9a–c). Notably, many *mt-Nd5* A12784G(3*) F_0 mice with higher initial editing efficiencies did not produce offspring mice with a 100% target site editing efficiency (Extended Data Fig. 9d). This suggests that the F_0 No. 8 mouse may possess unique traits resulting in the production of oocytes with 100% editing efficiency. Overall, these findings indicate that mtDNA edits from mitoBEs v2 can be maternally transmitted, potentially leading to mutant mice with a 100% target site mutation load, with variability in F_1 mutation loads probably due to the mtDNA genetic bottleneck[38].

F_1 mice born from *mt-Nd5* A12784G(3*) F_0 mice were distributed as follows: approximately 56% contained three mutation sites, 29.3% contained two mutations (A12780G and A12784G, or A12784G and A12786G), and 14.7% contained a single mutation (A12784G; Fig. 4h). This distribution may reflect the distribution of edited reads in the targeted region of F_0 mice (Extended Data Fig. 5d), which undergo a certain degree of separation in the offspring owing to the mtDNA genetic bottleneck. Notably, some *mt-Nd5* A12784G F_1 mice showed only the target site mutation, with a mutation load up to 49% (Fig. 4h). This is probably due to a high proportion of mtDNA copies in F_0 mice with only the target site edited (Extended Data Fig. 5d). Analysing the distribution of edited reads of the target region in two *mt-Nd5* A12784G F_1 mice revealed that 100% of the editing occurred at the target site 12784 (Extended Data Fig. 9e). This suggests that when a female mouse has a high proportion of mtDNA copies with only target site editing, it is likely to produce offspring with only target site editing owing to the mtDNA genetic bottleneck. Further breeding of these mice could yield *mt-Nd5* A12784G single-base-mutation mice with enhanced editing efficiency.

mt-Atp6 T8591C is lost during passaging

As previously noted, the birth rate of *mt-Atp6* T8591C(6*) F_0 mice was significantly lower than that of the control group (Fig. 3g). Injections were performed at the one-cell stage, suggesting that the six mutations within the *mt-Atp6* T8591C editing window may affect embryonic development. T8589C, T8595C and T8598C are synonymous mutations, whereas T8585C, T8587C and T8591C are missense mutations. Among these, the editing efficiency of site 8591 is much higher than that of 8585 and 8587. Given that the mtDNA mutation loads typically need to surpass a threshold of approximately 60% to induce disease phenotypes, it is speculated that the *mt-Atp6* T8591C mutation is harmful to embryonic development.

During mouse breeding, we observed that the target site mutation loads in most *mt-Atp6* T8591C(6*) F_1 mice were lower than those in their corresponding F_0 mothers, except for one mouse from *mt-Atp6* T8591C(6*) F_0 No. 10, which had a higher mutation load (Extended Data Fig. 10a). In the F_2 generation, only one litter of *mt-Atp6* T8591C(6*) mice had a target site mutation, averaging 11%, much lower than that of the F_1 mother with a 73% editing efficiency (Extended Data Fig. 10b). By contrast, *mt-Nd5* A12784G(3*) F_1 mice generally had higher mutation loads than their corresponding F_0 mothers, with only the litter of F_0 No. 17 showing a lower average (Extended Data Fig. 10c). All *mt-Nd5* A12784G(3*) F_2 mice had target site mutations, unlike the *mt-Atp6* T8591C(6*) F_2 mice (Extended Data Fig. 10b,d). This indicates that the inheritance of mtDNA mutations shows rapid shifts in heteroplasmy across generations[39].

Statistics on the number of F_1 and F_2 mice born per litter showed that the average number of births per litter of *mt-Atp6* T8591C(6*) F_1 mice was significantly lower than that of control mice, whereas there was no significant difference between *mt-Atp6* T8591C(6*) F_2, *mt-Nd5* A12784G(3*) F_1 and *mt-Nd5* A12784G(3*) F_2 versus control mice (Fig. 4i). This suggests that the *mt-Atp6* T8591C mutation may affect embryonic development after fertilization and/or the maturation of eggs before fertilization, resulting in a lower mutation load and fewer pups per litter in F_1 mice. When the T8591C mutation was eliminated in *mt-Atp6* T8591C(6*) F_2 mice, the number of pups per litter in F_2 mice increased compared to that in F_1 mice.

We utilized these two models to study the spread of mitochondrial heteroplasmy within the population, crossing three female F_0 mice with the *mt-Atp6* T8591C or *mt-Nd5* A12784G mutation with wild-type male mice from F_1 to F_3 generations. In each generation, we selected three female mice with the highest target site mutation loads and crossed them with wild-type male mice to obtain the next generation. We recorded the mutation rates of the two sites with the highest mutation load within the editing window in the F_0 to F_3 generation mice. For *mt-Atp6* T8591C(6*) mice, we recorded sites 8591 and 8595, where the T8591C mutation caused an amino acid change of Leu222Pro, and T8595C is a synonymous mutation. For *mt-Nd5* A12784G(3*) mice, we recorded sites 12780 and 12784, where A12780G and A12784G caused amino acid changes of Ile347Val and His348Arg, respectively.

As breeding progressed, the average target site mutation load of *mt-Atp6* T8591C(6*) F_1 mice was much lower than that of F_0 mice, with F_2 mice showing even lower levels (Fig. 4j). The adjacent synonymous mutation *mt-Atp6* T8595C also diminished from F_0 to F_2 generations (Fig. 4j), probably because the co-occurring frequency of both mutations on mtDNA copies is as high as about 90% (Extended Data Fig. 5c). The *mt-Atp6* T8591C mutation in the F_3 generation was almost completely lost, whereas the average mutation load of *mt-Atp6* T8595C even increased (Fig. 4j). This indicates that *mt-Atp6* T8595C mutation within the editing window with neutral effects on embryonic development may be retained or even increased when deleterious mutation *mt-Atp6* T8591C is substantially reduced. Conversely, *mt-Nd5* A12784G and the nearby *mt-Nd5* A12780G were retained across generations, with the average mutation load gradually increasing from F_0 to F_3 (Fig. 4k). Thus, T8591C seems more detrimental to mouse development than A12784G. The mtDNA genetic bottleneck contributes to greater selection pressure against T8591C, leading to its rapid loss over generations.

Mouse models exhibit disease phenotypes

We selected 12 *mt-Atp6* T8591C(6*) F_0 mice, aged 2 months, with editing efficiencies between 41% and 68% (Fig. 5a) and 6 age-matched control mice to evaluated heart rates. The *mt-Atp6* T8591C(6*) F_0 mice exhibited a significantly lower average heart rate compared to that of the control group (Fig. 5b). M-mode echocardiography revealed a notably reduced left ventricular ejection fraction in *mt-Atp6* T8591C(6*) F_0 mice compared to that of wild-type control mice (Fig. 5c). Obvious differences were also observed in echocardiographic comparisons between *mt-Atp6* T8591C(6*) F_0 No. 9 and the control (Fig. 5d). These mice have six mutation sites in the editing window (Fig. 5a). The T8589C, T8595C and T8598C are all synonymous mutations. For the three non-synonymous mutation sites, the average editing efficiency

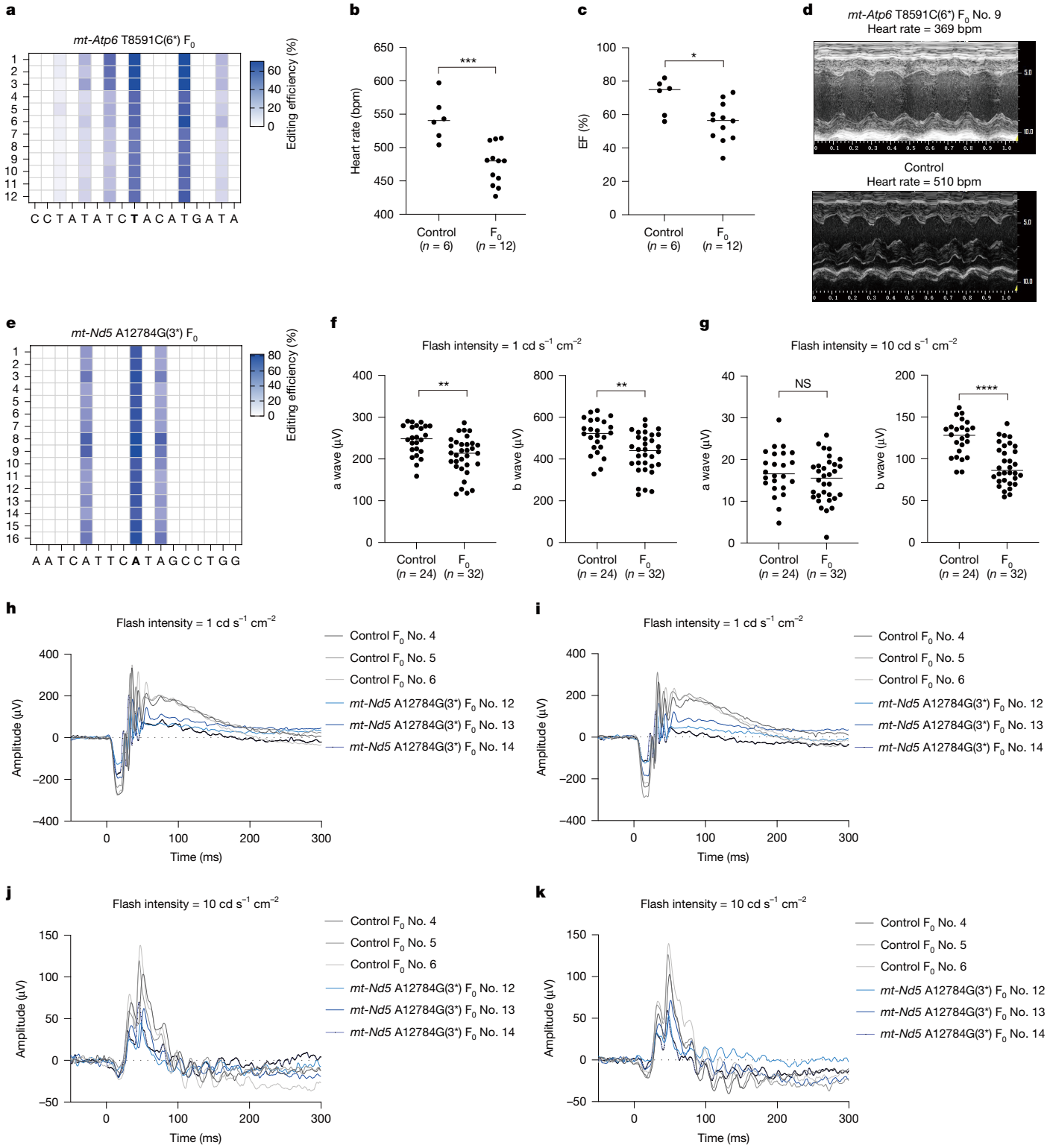

Fig. 5 | Disease phenotypes of *mt-Atp6* T8591C(6*) and *mt-Nd5* A12784G(3*) F_0 mice. a, Editing results within the editing window of *mt-Atp6* T8591C(6*) F_0 mice used for heart rate detection. Horizontal axis displays editing window and bold base indicating the target site 8591. **b**, Heart rate of control and *mt-Atp6* T8591C(6*) F_0 mice. **c**, Left ventricular ejection fraction (EF) of control and *mt-Atp6* T8591C(6*) F_0 mice. For **b** and **c**, number of mice $n = 6$ for control and 12 for F_0; centre lines, medians. **d**, Echocardiograms of *mt-Atp6* T8591C(6*) F_0 No. 9 and control mice. **e**, Editing results within the editing window of *mt-Nd5* A12784G(3*) F_0 mice used for ERG. Horizontal axis shows editing window and bold base indicating the target site 12784. **f**, Dark ERG for control and *mt-Nd5* A12784G(3*) F_0 mice. **g**, Light ERG for control and *mt-Nd5* A12784G(3*) F_0 mice. For **f** and **g**, number of eyes $n = 24$ for control and 32 for F_0; centre lines, medians. For **b**, **c**, **f** and **g**, the statistical test used was two-tailed Student's *t*-test, with *P* values of 0.0003 (***) for **b**, 0.0138 (*) for **c**, 0.0015 (**) and 0.0013 (**) for **f**, 0.2015 (>0.05, NS) and <0.0001 (****) for **g**. **h**, ERG curves of the left eyes of three *mt-Nd5* A12784G(3*) F_0 (No. 12, No. 13 and No. 14) and control (No. 4, No. 5 and No. 6) mice under dark adaptation. **i**, ERG curves of the right eyes of mice corresponding to **h** under dark adaptation. **j**, ERG curves of the left eyes of mice corresponding to **h** under light adaptation. **k**, ERG curves of the right eyes of mice corresponding to **h** under light adaptation.

of 8591 (about 50.4%) is much higher than that of 8585 (about 4.7%) and 8587 (about 15.7%). As mitochondrial mutation loads usually need to exceed a certain threshold before causing disease phenotypes, we speculate that the *mt-Atp6* T8591C mutation affects cardiac function, resembling symptoms observed in patients with Leigh syndrome[6].

For the *mt-Nd5* A12784G(3*) F_0 mice, we selected 16 mice, aged 1 month, with editing efficiencies ranging from 59% to 82% (Fig. 5e) and 12 age-matched control mice to conduct electroretinography (ERG) analysis. Under dark-adapted conditions, the average levels of the a-wave and b-wave responses in both eyes of *mt-Nd5* A12784G(3*) F_0 mice were significantly lower than those in control mice (Fig. 5f). In light-adapted conditions, the a-wave responses were similar between the groups, but the b-wave responses were significantly reduced in the *mt-Nd5* A12784G(3*) F_0 mice (Fig. 5g). ERG curves for three *mt-Nd5* A12784G(3*) (No. 12, No. 13 and No. 14) and control (No. 4, No. 5 and No. 6) mice showed clear photoreceptor abnormalities in the *mt-Nd5* A12784G(3*) F_0 mice (Fig. 5h–k). All three mutations within the editing window of these mice are non-synonymous and exhibit similar editing efficiencies. Consequently, we speculate that these three mutations impair the light-sensing capabilities of photoreceptor cells, leading to vision impairment similar to symptoms observed in patients with LHON[9].

In conclusion, we successfully used mitoBEs v2 for efficient mtDNA base editing at sites 8591 and 12784 in mice, corresponding to the human pathogenic mutations m.T9191C and m.A13379G. Mice with the high-efficiency T8591C mutation exhibited significant cardiac dysfunction, reflecting disease phenotypes linked to Leigh syndrome caused by the m.T9191C mutation[36]. Similarly, mice carrying the high-efficiency A12784G mutation exhibited decreased visual acuity, resembling LHON phenotypes associated with the m.A13379G mutation[37]. These findings highlight the effectiveness of mitoBEs v2 in creating mouse models of mitochondrial diseases, offering valuable tools for investigating the underlying mechanisms and developing potential therapies.

Establishing single-mutation mouse models

Owing to the presence of multiple editing sites within the editing window of the previous disease models, establishing a direct link between specific mutations and disease phenotypes remains challenging, even if the pathogenic mutations of *mt-Atp6* T8591C(6*) and *mt-Nd5* A12784G(3*) mice are narrowed down to three missense mutations. Therefore, we aimed to achieve editing exclusively at the target site by adjusting the TALE-binding positions of mitoBEs v2, using *mt-Nd5* A12784G as an example.

We screened circRNA-encoded mitoBE v2 pairs in Neuro-2a cells and found that some pairs could achieve single-base editing of target site, such as L2 + R6, L2 + R7, L5 + R6 and L5 + R7 (Extended Data Fig. 11a). We microinjected the L2 + R7 pair into mouse embryos, resulting in F_0 mice with up to 73% single-base-editing efficiency (Extended Data Fig. 11b). We selected six mutant mice and six age-matched control mice for ERG detection and found that the *mt-Nd5* A12784G F_0 mice showed symptoms of visual impairment similar to those observed in patients with LHON (Extended Data Fig. 11c–e). Therefore, the *mt-Nd5* A12784G single mutation impairs the photoreceptor cells' light-sensing capabilities, leading to vision impairment akin to symptoms observed in patients with LHON[37].

Discussion

mitoBEs are highly effective mitochondrial base editors with strand-selective capabilities, enabling precise A-to-G and C-to-T edits in mtDNA[1,20]. This versatility allows mitoBEs to model and potentially treat approximately 87% of known pathogenic mitochondrial mutations. To develop mouse models of mitochondrial diseases, RNA-expressed mitoBEs are injected into mouse zygotes. Compared to plasmid-encoded versions, mRNA-encoded mitoBEs demonstrated much higher editing efficiency and revealed off-target effects of mitoCBEs in the mitochondrial genome. Additionally, we observed transcriptome off-target effects with mitoABE (Extended Data Fig. 1). By engineering deaminases, we enhanced target site editing accuracy to create precise mitochondrial disease models. For mitoABEs, saturation mutagenesis of six key amino acids in TadA8e-V106W identified the V28F alteration, improving editing efficiency and reducing transcriptome off-target effects. For mitoCBEs, replacing APOBEC1 with 16 other cytosine deaminases revealed that CBE6d achieved higher editing efficiency and a narrower editing window with minimal off-target effects in the mitochondrial genome (Fig. 1). Neither the original nor the upgraded mitoBEs caused noticeable off-target effects in the nuclear genome (Extended Data Fig. 2 and Supplementary Tables 2 and 3).

Using mitoBEs v2, we screened 70 homologous sites in mouse cell lines corresponding to human pathogenic mtDNA mutations and successfully edited 68 sites, with 8 sites achieving around 20% editing efficiency (Fig. 2 and Extended Data Fig. 4). By microinjecting circRNA-encoded mitoBEs v2 into mouse embryos targeting *mt-Atp6* T8591C and *mt-Nd5* A12784G—analogous to human pathogenic mutations m.T9191C (associated with Leigh syndrome) and m.A13379G (associated with LHON)—we achieved editing efficiencies of up to 68% and 82% in F_0 mice (Fig. 3). We detected no off-target effects in either the mitochondrial or nuclear genomes, ensuring a clean genetic background for mitochondrial disease animal model development (Fig. 3, Extended Data Fig. 7 and Supplementary Table 5). Tissue analysis from 2- and 6-month-old mice showed that the editing effects persisted across development, indicating widespread and durable editing (Fig. 4 and Extended Data Fig. 8). The mitochondrial mutations were maternally inheritable, and notably, some *mt-Nd5* A12784G(3*) F_1 mice showed 100% target site mutation, suggesting that mitoBEs v2 and selective breeding could yield mice with 100% mtDNA mutations, assuming that the mutation does not impair embryonic development (Fig. 4 and Extended Data Fig. 9). Unlike DdCBEs and TALEDs achieving only about 10% on-target editing efficiency in F_0 mice[40,41], mitoBEs v2 offer much higher editing efficiency, specificity and better mimicry of human mitochondrial diseases.

As mouse breeding progressed, we observed that the *mt-Atp6* T8591C mutation may affect embryonic development or egg maturation (Figs. 3 and 4). This mutation was quickly lost during breeding, providing insights into the propagation of mitochondrial heteroplasmy in populations (Fig. 4 and Extended Data Fig. 10). These findings highlight the high editing efficiency of mitoBEs v2 in F_0 generation mice, along with the stability of circRNA encoding.

Most mitochondrial diseases arise from point mutations in mitochondrial genes, with disease phenotypes manifesting only after the mutated mitochondrial genome surpasses a certain threshold. For instance, LHON typically leads to blindness with a mutation load exceeding 60% (ref. 42), although a 40% mutation load of m.A13379G can also trigger the disease[43]. Our mouse models show high editing efficiencies (42–82%) at targeted sites, closely replicating the disease phenotypes. Phenotypic assessments confirmed that our *mt-Atp6* T8591C and *mt-Nd5* A12784G models effectively mimic Leigh syndrome and LHON, respectively (Fig. 5). Additionally, mitoBEs v2 have enabled the creation of other mitochondrial disease mouse models with high editing efficiency (Fig. 3 and Extended Data Fig. 6), warranting further exploration of their associated phenotypes. These models provide a valuable platform for studying disease mechanisms and testing therapeutic strategies.

The ideal scenario for developing mouse models of mitochondrial mutations is achieving efficient editing at the target site while avoiding unintended edits elsewhere in the editing window. We achieved single-base editing at site 12784 by adjusting the positions of the TALEs (Extended Data Fig. 11), which holds potential for generating more single-mutation mouse models by evaluating editing outcomes in the

Neuro-2a cell line (Extended Data Fig. 4), such as *mt-TrnF* G7A, *mt-Nd1* G3177A and *mt-TrnI* G3751A. However, achieving single-base editing is more challenging when the target site is adjacent to unintended editing sites. We also identified F_1 generation mice with exclusive editing at the target site 12784 (Fig. 4), and by selectively breeding these female mice with wild-type males, we can produce *mt-Nd5* A12784G mice with a higher mutation efficiency. For cases in which single-base editing is difficult, hybridization isolation may offer a solution.

Looking ahead, the therapeutic potential of mitoBEs v2 is promising, especially with delivery systems such as adeno-associated virus or lipid nanoparticles. Specifically, mitoCBE v2 can address diseases stemming from A-to-G (T-to-C) mutations, whereas mitoABE v2 is suited to address C-to-T (G-to-A) mutations. These models will advance both research and treatment strategies for mitochondrial diseases.

Online content

Any methods, additional references, Nature Portfolio reporting summaries, source data, extended data, supplementary information, acknowledgements, peer review information; details of author contributions and competing interests; and statements of data and code availability are available at https://doi.org/10.1038/s41586-024-08469-8.

1. Yi, Z. et al. Strand-selective base editing of human mitochondrial DNA using mitoBEs. *Nat. Biotechnol.* **42**, 498–509 (2024).
2. Brandon, M. C. et al. MITOMAP: a human mitochondrial genome database–2004 update. *Nucleic Acids Res.* **33**, D611–D613 (2005).
3. Greaves, L. C., Reeve, A. K., Taylor, R. W. & Turnbull, D. M. Mitochondrial DNA and disease. *J. Pathol.* **226**, 274–286 (2012).
4. Ng, Y. S. & Turnbull, D. M. Mitochondrial disease: genetics and management. *J. Neurol.* **263**, 179–191 (2016).
5. Lightowlers, R. N., Chinnery, P. F., Turnbull, D. M. & Howell, N. Mammalian mitochondrial genetics: heredity, heteroplasmy and disease. *Trends Genet.* **13**, 450–455 (1997).
6. Finsterer, J. Leigh and Leigh-like syndrome in children and adults. *Pediatr. Neurol.* **39**, 223–235 (2008).
7. Wallace, D. C. et al. Mitochondrial DNA mutation associated with Leber's hereditary optic neuropathy. *Science* **242**, 1427–1430 (1988).
8. Baertling, F. et al. A guide to diagnosis and treatment of Leigh syndrome. *J. Neurol. Neurosurg. Psychiatry* **85**, 257–265 (2014).
9. Meyerson, C., Van Stavern, G. & McClelland, C. Leber hereditary optic neuropathy: current perspectives. *Clin. Ophthalmol.* **9**, 1165–1176 (2015).
10. Rahman, S. Mitochondrial disease in children. *J. Intern. Med.* **287**, 609–633 (2020).
11. La Morgia, C., Maresca, A., Caporali, L., Valentino, M. L. & Carelli, V. Mitochondrial diseases in adults. *J. Intern. Med.* **287**, 592–608 (2020).
12. Magner, M., Kolarova, H., Honzik, T., Svandova, I. & Zeman, J. Clinical manifestation of mitochondrial diseases. *Dev. Period Med.* **19**, 441–449 (2015).
13. Wallace, D. C. Mouse models for mitochondrial disease. *Am. J. Med. Genet.* **106**, 71–93 (2001).
14. Stewart, J. B. Current progress with mammalian models of mitochondrial DNA disease. *J. Inherit. Metab. Dis.* **44**, 325–342 (2021).
15. Zhang, D. et al. Construction of transgenic mice with tissue-specific acceleration of mitochondrial DNA mutagenesis. *Genomics* **69**, 151–161 (2000).
16. Bacman, S. R., Williams, S. L., Pinto, M., Peralta, S. & Moraes, C. T. Specific elimination of mutant mitochondrial genomes in patient-derived cells by mitoTALENs. *Nat. Med.* **19**, 1111–1113 (2013).
17. Gammage, P. A., Rorbach, J., Vincent, A. I., Rebar, E. J. & Minczuk, M. Mitochondrially targeted ZFNs for selective degradation of pathogenic mitochondrial genomes bearing large-scale deletions or point mutations. *EMBO Mol. Med.* **6**, 458–466 (2014).
18. Mok, B. Y. et al. A bacterial cytidine deaminase toxin enables CRISPR-free mitochondrial base editing. *Nature* **583**, 631–637 (2020).
19. Cho, S. I. et al. Targeted A-to-G base editing in human mitochondrial DNA with programmable deaminases. *Cell* **185**, 1764–1776 (2022).
20. Zhang, X. & Wei, W. CRISPR-free, strand-selective mitochondrial DNA base editing using a nickase. *Nat. Biotechnol.* **42**, 392–393 (2024).
21. Harris, R. S., Petersen-Mahrt, S. K. & Neuberger, M. S. RNA editing enzyme APOBEC1 and some of its homologs can act as DNA mutators. *Mol. Cell* **10**, 1247–1253 (2002).
22. Saraconi, G., Severi, F., Sala, C., Mattiuz, G. & Conticello, S. G. The RNA editing enzyme APOBEC1 induces somatic mutations and a compatible mutational signature is present in esophageal adenocarcinomas. *Genome Biol.* **15**, 417 (2014).
23. Tunyasuvunakool, K. et al. Highly accurate protein structure prediction for the human proteome. *Nature* **596**, 590–596 (2021).
24. Losey, H. C., Ruthenburg, A. J. & Verdine, G. L. Crystal structure of *Staphylococcus aureus* tRNA adenosine deaminase TadA in complex with RNA. *Nat. Struct. Mol. Biol.* **13**, 153–159 (2006).
25. Grunewald, J. et al. CRISPR DNA base editors with reduced RNA off-target and self-editing activities. *Nat. Biotechnol.* **37**, 1041–1048 (2019).
26. Ma, Y. et al. Targeted AID-mediated mutagenesis (TAM) enables efficient genomic diversification in mammalian cells. *Nat. Methods* **13**, 1029–1035 (2016).
27. Thuronyi, B. W. et al. Continuous evolution of base editors with expanded target compatibility and improved activity. *Nat. Biotechnol.* **37**, 1070–1079 (2019).
28. Gehrke, J. M. et al. An APOBEC3A-Cas9 base editor with minimized bystander and off-target activities. *Nat. Biotechnol.* **36**, 977–982 (2018).
29. Wang, X. et al. Efficient base editing in methylated regions with a human APOBEC3A-Cas9 fusion. *Nat. Biotechnol.* **36**, 946–949 (2018).
30. Neugebauer, M. E. et al. Evolution of an adenine base editor into a small, efficient cytosine base editor with low off-target activity. *Nat. Biotechnol.* **41**, 673–685 (2023).
31. Chen, L. et al. Re-engineering the adenine deaminase TadA-8e for efficient and specific CRISPR-based cytosine base editing. *Nat. Biotechnol.* **41**, 663–672 (2023).
32. Zhang, E., Neugebauer, M. E., Krasnow, N. A. & Liu, D. R. Phage-assisted evolution of highly active cytosine base editors with enhanced selectivity and minimal sequence context preference. *Nat. Commun.* **15**, 1697 (2024).
33. Grau, J., Boch, J. & Posch, S. TALENoffer: genome-wide TALEN off-target prediction. *Bioinformatics* **29**, 2931–2932 (2013).
34. Wesselhoeft, R. A., Kowalski, P. S. & Anderson, D. G. Engineering circular RNA for potent and stable translation in eukaryotic cells. *Nat. Commun.* **9**, 2629 (2018).
35. Qu, L. et al. Circular RNA vaccines against SARS-CoV-2 and emerging variants. *Cell* **185**, 1728–1744 (2022).
36. Su, X. et al. Molecular basis of the pathogenic mechanism induced by the m.9191T>C mutation in mitochondrial ATP6 gene. *Int. J. Mol. Sci.* https://doi.org/10.3390/ijms21145083 (2020).
37. Peverelli, L. et al. Leber's hereditary optic neuropathy: a report on novel mtDNA pathogenic variants. *Front. Neurol.* **12**, 657317 (2021).
38. Zhang, H., Burr, S. P. & Chinnery, P. F. The mitochondrial DNA genetic bottleneck: inheritance and beyond. *Essays Biochem.* **62**, 225–234 (2018).
39. Fan, W. et al. A mouse model of mitochondrial disease reveals germline selection against severe mtDNA mutations. *Science* **319**, 958–962 (2008).
40. Silva-Pinheiro, P. et al. A library of base editors for the precise ablation of all protein-coding genes in the mouse mitochondrial genome. *Nat. Biomed. Eng.* **7**, 692–703 (2023).
41. Cho, S. I. et al. Engineering TALE-linked deaminases to facilitate precision adenine base editing in mitochondrial DNA. *Cell* **187**, 95–109 (2024).
42. Yu-Wai-Man, P., Turnbull, D. M. & Chinnery, P. F. Leber hereditary optic neuropathy. *J. Med. Genet.* **39**, 162–169 (2002).
43. Krylova, T. D. et al. Three rare pathogenic mtDNA substitutions in LHON patients with low heteroplasmy. *Mitochondrion* **50**, 139–144 (2020).

Methods

Plasmid construction

PCR was performed using either PrimeSTAR GXL DNA polymerase (TaKaRa) or Q5 Hot Start High-Fidelity DNA Polymerase (NEB). Genes expressing TadA mutants, APOBEC1, UGI, MutH, Nt.BspD6I(C), AID, evoAPOBEC1, evoCDA1, hA3A, evoFERNY and other proteins were synthesized as gene blocks optimized for mammalian expression codons (Beijing Tsingke Biotech). The corresponding amino acid sequences are listed in Supplementary Table 6. Original mitoBEs expression plasmids were assembled into the pCMV vector using Gibson assembly, incorporating two inverted BsmBI restriction sites in place of the TALE array. Subsequently, the TALE array was constructed using the advanced ULtiMATE system[44–46] (see Supplementary Table 7 for all TALE array recognition sequences in this manuscript). The ligated plasmids were transformed into Trans1-T1 chemically competent cells (TransGene Biotech) and confirmed by Sanger sequencing (Beijing Tsingke Biotech). Final plasmids were prepared (TianGen) for cell transfection.

RNA preparation

mRNA was prepared using E2060 reagent kit (NEB) according to the manufacturer's protocol. circRNAs were prepared following established protocols[34,35]. In summary, precursor circRNAs were synthesized from linearized circRNA plasmid templates through in vitro transcription using the HiScribe T7 High Yield RNA Synthesis Kit (NEB). Products were treated with DNase I (NEB) for 30 min to degrade the plasmid templates. Following DNase I digestion, GTP was added to a final concentration of 2 mM and incubated at 55 °C for 15 min to facilitate circRNA cyclization. RNA was then purified using RNA Clean & Concentrator-25 (Zymo Research), heated at 65 °C for 3 min, and rapidly cooled on ice. To enrich circRNAs, RNase R (Epicentre) treatment was performed at 37 °C for 15–30 min, followed by another round of purification using RNA Clean & Concentrator-25 (Zymo Research).

Cell culture and transfection

HEK293T (ATCC, CRL-3216) was from C. Zhang's laboratory (Peking University) and Neuro-2a (ATCC, CCL-131) cells were purchased from Pricella, and cell lines were authenticated using STR analysis and tested negative for mycoplasma contamination. They were cultured in Dulbecco's modified Eagle's medium (Gibco) with 10% fetal bovine serum (Biological Industries), 1% GlutaMax (Gibco) and penicillin–streptomycin (Sigma) at 37 °C with 5% CO_2. For lipofection, cells were plated in 12-well cell culture plates to reach approximately 70% confluence after 20 h. Cells in each well were transfected with 2,000 ng of each mitoBEs monomer plasmid using 8 µl of PEI (Protein-Tech) or with 2,500 ng of each mitoBEs monomer mRNA or circRNA using 5 µl of Lipofectamine MessengerMAX Reagent (Invitrogen). Cells were collected after 72 h post-transfection. Genomic DNA was extracted using the DNeasy Blood & Tissue Kit (Qiagen) and stored at −20 °C.

Mouse

Mouse embryos used were C57BL/6J strains. In this study, all samples were allocated into experimental groups randomly. All mice were kept in a specific-pathogen-free animal room with temperatures controlled at 22–24 °C and relative humidity controlled at 30–70% under a 12-h dark–light cycle.

Ethics statement

This study was approved by the Institutional Animal Care and Use Committee and the Animal Ethics Committee of Cyagen Biosciences. All mouse experiments were performed at Cyagen Biosciences Inc (Project Number: TGBS230525JY3-S).

Microinjection of mitoBEs into mouse zygotes

Female C57BL/6J mice aged 3–4 weeks were injected with pregnant mare serum gonadotropin and human chorionic gonadotropin 46–48 h apart. Following injection of human chorionic gonadotropin, females were mated with fertile males to induce fertilization. The next day, females were euthanized, and fertilized eggs were collected from oviducts and incubated at 37 °C with 5% CO_2. RNA was loaded into microinjection needles, and normal fertilized eggs were transferred to injection dishes. RNA was microinjected into the cytoplasm under an inverted microscope at ×200–400 magnification. Injected eggs were cultured in M16 medium at 37 °C with 5% CO_2 for 0.5–1 h before transplantation, or until the two-cell stage for next-day transplantation. Surrogate mothers were housed in clean cages post-transplantation, with offspring typically born 19–20 days later.

Mouse genotyping

For genotyping of embryos and F_0 mice, embryos or F_0 mice injected only with buffer in one-cell stage served as controls. At 1 week after birth, toe samples were collected from mice to assess target site editing efficiency. Mouse toes (about 2 mm) were collected and placed in tubes with 98 µl Triton lysis buffer and 2 µl 20 mg ml^{-1} proteinase K. Tubes were incubated at 56 °C overnight, and then heated to 98 °C for 15 min to deactivate the proteinase K. Samples were then centrifuged, and supernatants were collected as PCR templates. Genomic regions of interest were amplified and sequenced using Fast NGS (Beijing Tsingke Biotech) for genotype identification. GraphPad Prism 8 was used for basic statistical analysis and graph production. The distribution of edited reads in the targeted region was calculated by CRISPResso2 (ref. 47).

Targeted deep sequencing

Genomic regions of interest were amplified into approximately 200-bp fragments from genomic DNA using PrimeSTAR GXL DNA polymerase (TaKaRa). See Supplementary Table 8 for primers. Amplified products were purified using the DNA Clean & Concentrator-25 (Zymo Research) kit for Sanger sequencing and targeted deep sequencing. For library preparation, the VAHTS Universal DNA Library Prep Kit for Illumina V3 (Vazyme) was used. PCR fragments underwent sequential processes including end repair, adaptor ligation and PCR amplification. DNA purification during library preparation was executed using Agencourt Ampure XP beads (Beckman Coulter), and library amplification used Q5U Hot Start High-Fidelity DNA Polymerase (NEB) and VAHTS Multiplex Oligos Set 4/5 for Illumina (Vazyme). The final library underwent quantification utilizing the Qubit dsDNA HS assay kit (Invitrogen) before being subjected to sequencing on the Illumina HiSeq X Ten platform.

Genome-wide off-target sequencing

Library preparation utilizing the VAHTS Universal Plus DNA Library Prep Kit for Illumina (Vazyme) required 500–1,000 ng of genomic DNA. The library preparation procedure involved the following steps: DNA fragmentation, end preparation with dA-tailing, adaptor ligation and library amplification. Fragmentation was achieved with FEA enzyme mix at 37 °C for 10 min. Following library preparation, the final libraries were quantified with the Qubit dsDNA HS assay kit (Invitrogen) and sequenced on the Illumina HiSeq X Ten platform (Illumina).

Transcriptome-wide off-target sequencing

HEK293T cells were transfected with either eGFP-expressing or mitoBEs-expressing plasmid or RNA. At 72 h post-transfection, RNA extraction was performed using Direct-zol RNA Miniprep Kits (Zymo Research). Subsequently, RNA was isolated using Ribo-off rRNA Depletion Kit (H/M/R) (Vazyme) and processed with the Universal V6 RNA-seq Library Prep Kit for Illumina (Vazyme). The prepared samples underwent deep sequencing analysis on the Illumina HiSeq X Ten platform.

Analysis of high-throughput sequencing data for targeted amplicon sequencing

To analyse high-throughput sequencing data, an index was created utilizing the targeted site sequences, covering approximately 100 nucleotides upstream and downstream of editing window regions. Subsequently, reads were aligned and quantified using BWA (v.0.7.10-r789). The resulting BAM alignment files underwent sorting with SAMtools (v1.1), and analysis of editing sites was conducted using REDitools (v.1.0.4)[48]. The applied parameters were: -t 8 -U [AG] -n 0.0 -T 6-6 -e -d -u. Any significant base conversions detected within the targeted regions, determined by Fisher's exact test (P value < 0.05), were identified as edits induced by mitoBEs. Mutations observed simultaneously in both control and experimental groups were considered attributable to single nucleotide polymorphisms.

Analysis of mitochondrial genome off-target editing

Whole-genome sequencing underwent quality control assessment using FastQC (v0.12.1), followed by adaptor removal with fastp (0.23.2). Following trimming, reads were aligned to GRCh38-hg38 or GRCm39-mm39 using bwa-mem2 (2.2.1) with default parameters. Subsequently, reads were mapped to GRCh38-hg38 or GRCm39-mm39 by bwa-mem2 (2.2.1) with default parameters. GATK (4.3.0.0)[49] AddOrReplaceReadGroups, MarkDuplicates and BaseRecalibrator were subsequently used to add read group, remove duplicates and correct base quantity. After preprocessing, GATK Mutect2 was used to discover somatic short variants. Variant calls were filtered according to FilterMutectCalls (not annotated as position, slippage, weak evidence or mapping quality). Mutations with a frequency of more than 1% in the control experiments were also removed.

Analysis of nuclear genome off-target editing

To assess potential off-target editing events in the human nuclear genome, we implemented stringent criteria to address noise levels. For mitoABE tools, we utilized the untreated group and mitoCBE group as controls. Conversely, for mitoCBE tools, we used the untreated group and mitoABE group as controls. We introduced additional quality control measures, requiring a minimum read depth of 30 and a median base quality (MBQ) of 30 across all experimental groups. To ensure robustness, only mutation sites detected consistently across all three replicates of the experimental group were classified as single nucleotide polymorphisms. These sites were used to plot the correlation between the control group and the experimental group, as well as to conduct differential analysis and create a volcano plot. The differential analysis follows the standard limma (v3.56.2)[50] pipeline. Only sites exhibiting a mutation rate below 1% in the control group were considered genuine off-target sites. These sites are presented in the off-target jitter plot. In pursuit of potential off-target editing events in the nuclear genome of mice, we used the same analysis strategy as for humans, in which we used a read depth value of 20 and an MBQ value of 26. Only sites exhibiting a mutation rate below 10% in the control group were considered genuine off-target sites.

For TALE-dependent off-target analysis, we used the TALENoffer tool for prediction, selected the top 500 sites as potential off-target sites, taking the site with the highest mutation rate in the editing window to represent the mutation rate for this potential off-target site.

Analysis of transcriptome off-target editing

The quality control of RNA-sequencing data was carried out as previously outlined. Alignments were executed using the two-pass mode of STAR (v2.7.11a), and variant calling was conducted in accordance with the standard GATK pipeline. Mutations with a frequency of more than 1% in the control experiments were also removed. To ensure high confidence in the variants identified from RNA-sequencing data, we use a combination of MBQ, median mapping quality and P value indicators to minimize the false positive rate. The Mann–Whitney U-test was implemented for group comparisons.

Analysis of genome coverage

We split the PCR duplicate-removed BAM file into nuclear and mitochondrial genomes using samtools. For calculating the depth of the nuclear genome, we used the window mode of the sambamba depth tool (v0.6.6) with the parameter -w 100000. For calculating the depth of the mitochondrial genome, we used the base mode of the same tool.

Phenotypic assessment of mouse

For phenotypic assessment, wild-type and mtDNA-mutant mice were mixed into cages, and experiments were conducted blinded. Sex was not considered in study design. For heart rate detection, animals were pre-anaesthetized in an anaesthesia chamber for 2 min, followed by positioning in a supine position on the electrode plate of the Indus Rodent Surgical MonitorY+. The limbs of the mice were secured, and continuous anaesthesia (1–2% isoflurane) was maintained at 37 °C while initiating heart rate monitoring software (labchart) to record data. For ultrasound imaging, mice were first anaesthetized, followed by correct placement in SiliconWave 30 electrodes for proper data acquisition. Three consecutive cardiac cycles were continuously recorded to obtain cardiac functional parameters (VEVO 770 software). For ERG testing, the Diagnosys Celeris instrument (Espion V6 software) was used. The sequence of ERG assessments included dark-adapted and light-adapted a-wave and b-wave testing. Before testing, animals were anaesthetized with intraperitoneal injections of pentobarbital sodium (50 mg kg^{-1}) and chlorpromazine hydrochloride injection (5 mg kg^{-1}).

Statistics and reproducibility

n represents the number of independent experiments performed in parallel. Unpaired two-tailed Student's t-test, Pearson's correlation coefficient and the Mann–Whitney U-test were implemented for group comparisons as indicated in the figure legends. NS, $P > 0.05$; *$P < 0.05$; **$P < 0.01$; ***$P < 0.001$; ****$P < 0.0001$. In this study, all sample sizes used met the requirements of their corresponding statistical test methods. For editing efficiency and off-target analyses of the HEK293T cell line, three independent experiments were performed for the target or control groups.

Reporting summary

Further information on research design is available in the Nature Portfolio Reporting Summary linked to this article.

Data availability

Raw data for off-target analysis are available as a BioProject with the project identifier PRJCA026376 in the China National Center for Bioinformation–National Genomics Data Center database (accessible via https://ngdc.cncb.ac.cn/bioproject/browse/PRJCA026376). The confirmed human disease-related mtDNA mutations in Supplementary Table 4 are available from the MITOMAP database (accessible via https://www.mitomap.org/MITOMAP). The data from the human genome assembly GRCh38-hg38 and the mouse genome assembly GRCm39-mm39 used in this study are available from the Gencode database (accessible via https://ftp.ebi.ac.uk/pub/databases/gencode). Source data are provided with this paper.

44. Zhang, Y. et al. Deciphering TAL effectors for 5-methylcytosine and 5-hydroxymethylcytosine recognition. *Nat. Commun.* **8**, 901 (2017).
45. Yang, J. et al. Complete decoding of TAL effectors for DNA recognition. *Cell Res.* **24**, 628–631 (2014).
46. Yang, J. et al. ULtiMATE system for rapid assembly of customized TAL effectors. *PLoS ONE* **8**, e75649 (2013).
47. Clement, K. et al. CRISPResso2 provides accurate and rapid genome editing sequence analysis. *Nat. Biotechnol.* **37**, 224–226 (2019).

48. Picardi, E. & Pesole, G. REDItools: high-throughput RNA editing detection made easy. *Bioinformatics* **29**, 1813–1814 (2013).
49. Van der Auwera, G. A. et al. From FastQ data to high confidence variant calls: the Genome Analysis Toolkit best practices pipeline. *Curr. Protoc. Bioinformatics* **43**, 11.10.11–11.10.33 (2013).
50. Ritchie, M. E. et al. limma powers differential expression analyses for RNA-sequencing and microarray studies. *Nucleic Acids Res.* **43**, e47 (2015).

Acknowledgements This project was financed by various sources, including Changping Laboratory, the National Science Foundation of China (NSFC82341207 and NSFC31930016) and the Peking-Tsinghua Center for Life Sciences (to W.W.). Additional support was provided by the China Postdoctoral Science Foundation Fellowship (No. 2022TQ0006 to Z.Y.).

Author contributions W.W. supervised the project, and Xiaoxue Zhang, Z.Y. and W.W. conceptualized the idea and designed the experiments. Xiaoxue Zhang and Xue Zhang conducted the experiments, with assistance from J.L. and X.W. Y.Y. prepared the samples for next-generation sequencing, and J.R. analysed the sequencing data. Xiaoxue Zhang, Z.Y. and W.W. wrote the manuscript, with input from all team members.

Competing interests A patent application (International Application No. PCT/CN2024/102318) based on the research described in this study has been filed. The inventors listed on the patent are W.W., Xiaoxue Zhang and Z.Y. W.W. is a scientific adviser and founder of EdiGene and Therorna. The other authors declare no competing interests.

Additional information

Supplementary information The online version contains supplementary material available at https://doi.org/10.1038/s41586-024-08469-8.

Correspondence and requests for materials should be addressed to Zongyi Yi or Wensheng Wei.

Peer review information *Nature* thanks Carlos Moraes and the other, anonymous, reviewer(s) for their contribution to the peer review of this work.

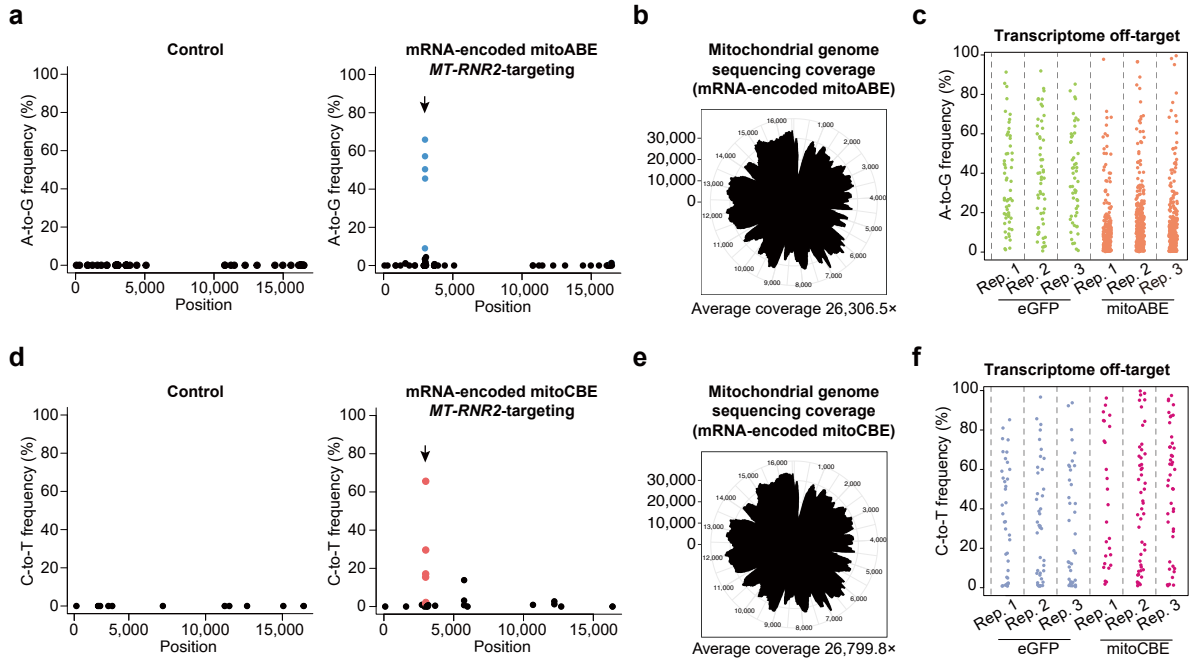

Extended Data Fig. 1 | Off-target assessment of mRNA-encoded mitoBEs on mitochondrial genome and transcriptofme. a, The average A-to-G mutation frequency on the mitochondrial genome is shown for untreated HEK293T cells (left) and HEK293T cells treated with mRNA-encoded *MT-RNR2*-targeting mitoABE (right). Editing efficiency was assessed 3 days post mRNA transfection. **b**, The average mitochondrial genome sequencing coverage for mRNA-encoded *MT-RNR2*-targeting mitoABE. **c**, The average A-to-G mutation frequency on the transcriptome of HEK293T cells transfected with mRNA-encoded eGFP and *MT-RNR2*-targeting mitoABE. **d**, The average C-to-T mutation frequency on the mitochondrial genome is shown for untreated HEK293T cells (left) and HEK293T cells treated with mRNA-encoded *MT-RNR2*-targeting mitoCBE (right). Editing efficiency was assessed 3 days post mRNA transfection. For **a** and **d**, three biological replicates were performed, yielding consistent results. The arrows indicate the targeted editing sites, with blue or red dots representing the editing of adenines or cytosines within the editing window. **e**, The average mitochondrial genome sequencing coverage for mRNA-encoded *MT-RNR2*-targeting mitoCBE. For **b** and **e**, data are presented as mean from $n = 3$ independent biological replicates. **f**, The average C-to-T mutation frequency on the transcriptome of HEK293T cells transfected with mRNA-encoded eGFP and *MT-RNR2*-targeting mitoCBE.

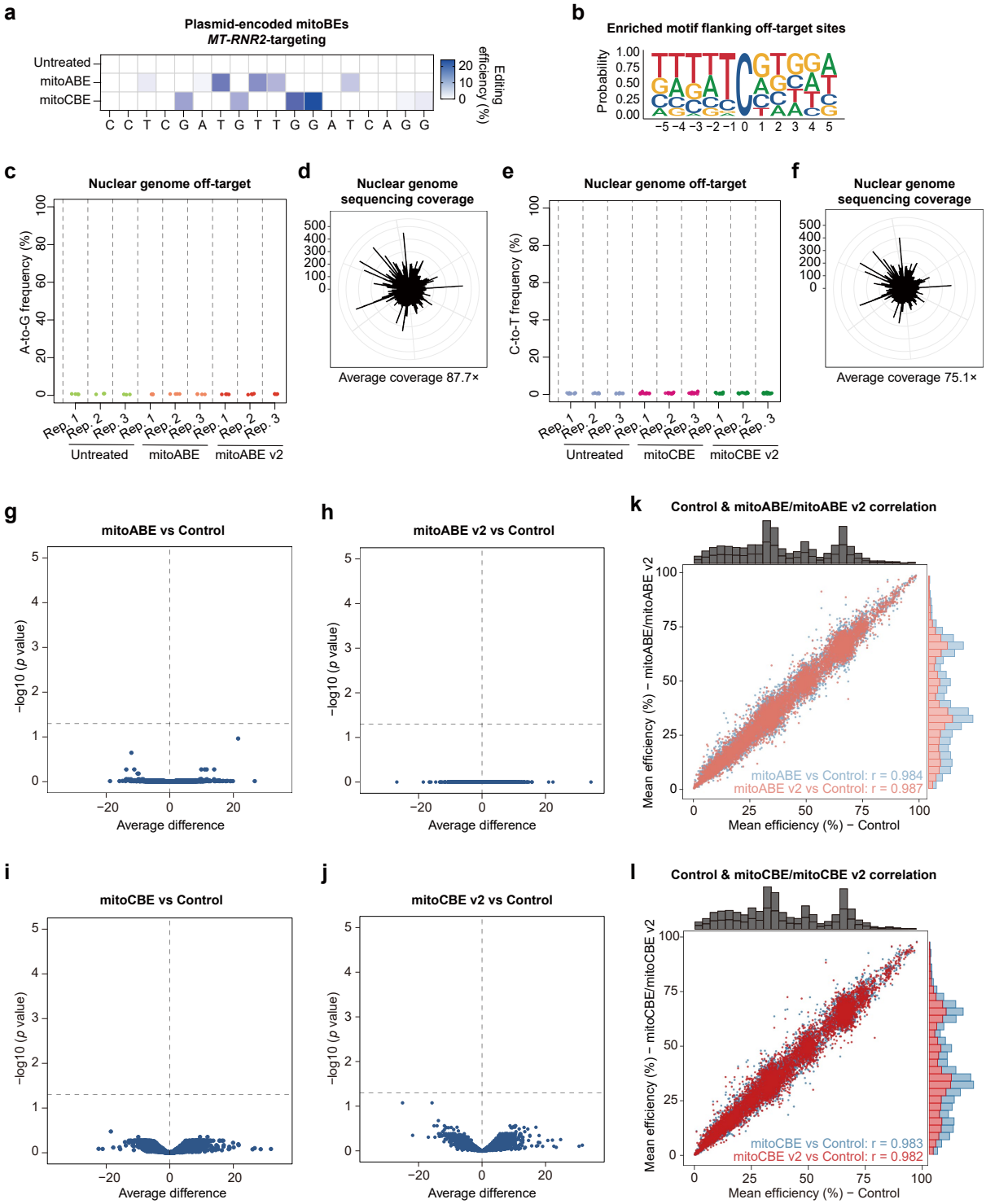

Extended Data Fig. 2 | Off-target assessment of mRNA-encoded original and upgraded mitoBEs on nuclear genome. a, Editing efficiency of plasmid-encoded mitoBEs at the *MT-RNR2* site, measured 3 days after transfection. Data are presented as mean from $n = 3$ independent biological replicates. **b**, Motif analysis of flanking sequences for mRNA-encoded *MT-RNR2*-targeting mitoCBE off-target sites on the mitochondrial genome. **c**, Nuclear off-target effects of mitoABE and mitoABE v2. **d**, Average nuclear genome sequencing coverage for samples corresponding to **c**. **e**, Nuclear off-target effects of mitoCBE and mitoCBE v2. **f**, Average nuclear genome sequencing coverage for samples corresponding to **e**. **g**-**j**, Volcano plots of differential site analysis between mitoABE and control (**g**), mitoABE v2 and control (**h**), mitoCBE and control (**i**), and mitoCBE v2 and control (**j**). The horizontal dashed line represents p-value = 0.05. Three independent experiments were performed. The p-value is based on a two-tailed Student's t-test corrected for multiple comparisons, implemented using the R package limma. **k**, Analysis of nuclear genome off-target effects of mitoABE and mitoABE v2 using whole-genome sequencing. Pearson's correlation coefficient was used to assess the differential editing rate between mitoABE or mitoABE v2 and control. **l**, Analysis of nuclear genome off-target effects of mitoCBE and mitoCBE v2 using whole-genome sequencing. Pearson's correlation coefficient was used to assess the differential editing rate between mitoCBE or mitoCBE v2 and control. For **k** and **l**, each point represents a SNP site. The horizontal axis shows average mutation rates. Marginal plots display rate distributions. Three independent experiments were performed.

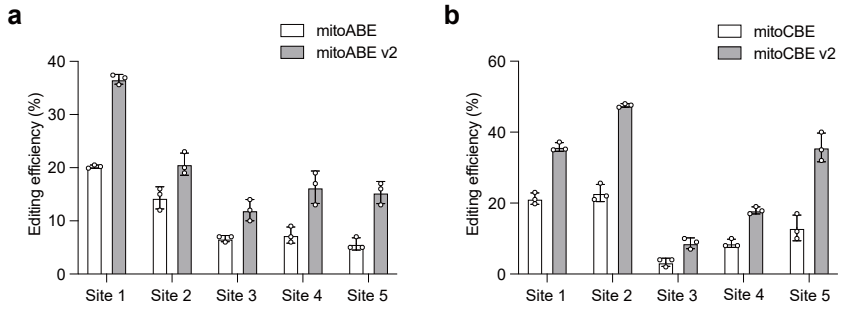

Extended Data Fig. 3 | Comparison of editing efficiency between the original and upgraded mitoBEs in HEK293T cells. a, Editing efficiency of mitoABE and mitoABE v2 at various sites. **b**, Editing efficiency of mitoCBE and mitoCBE v2 at various sites. For both **a** and **b**, editing efficiency was measured 3 days post-transfection in HEK293T cells. Data are presented as mean ± s.d. from $n = 3$ independent biological replicates.

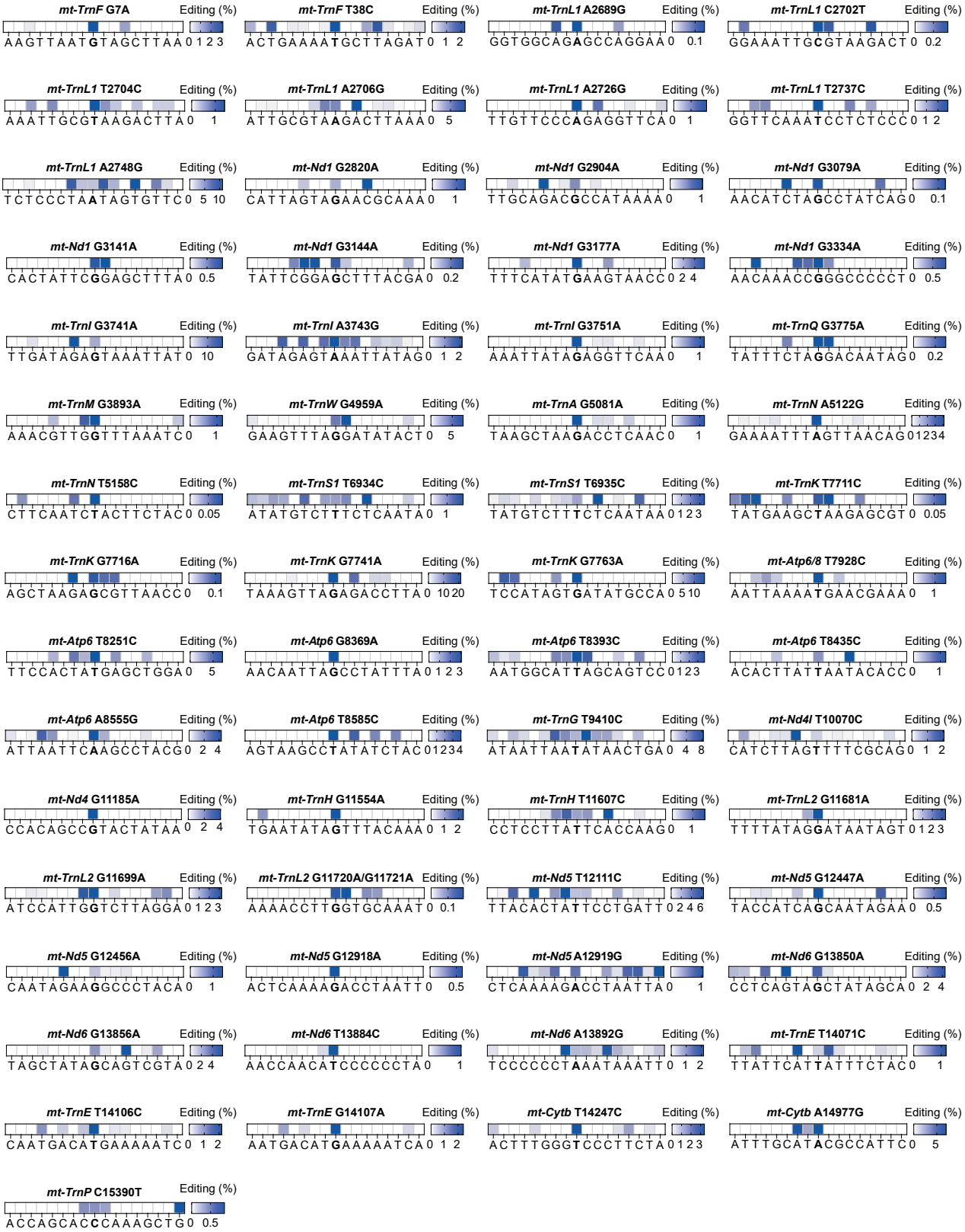

Extended Data Fig. 4 | Editing efficiency of circRNA-encoded mitoBEs v2 in Neuro-2a cells at multiple sites. The horizontal axis displays 17 bases within the editing window, with the bold base in the middle position indicating the target site. Data are presented as mean from $n = 3$ independent biological replicates.

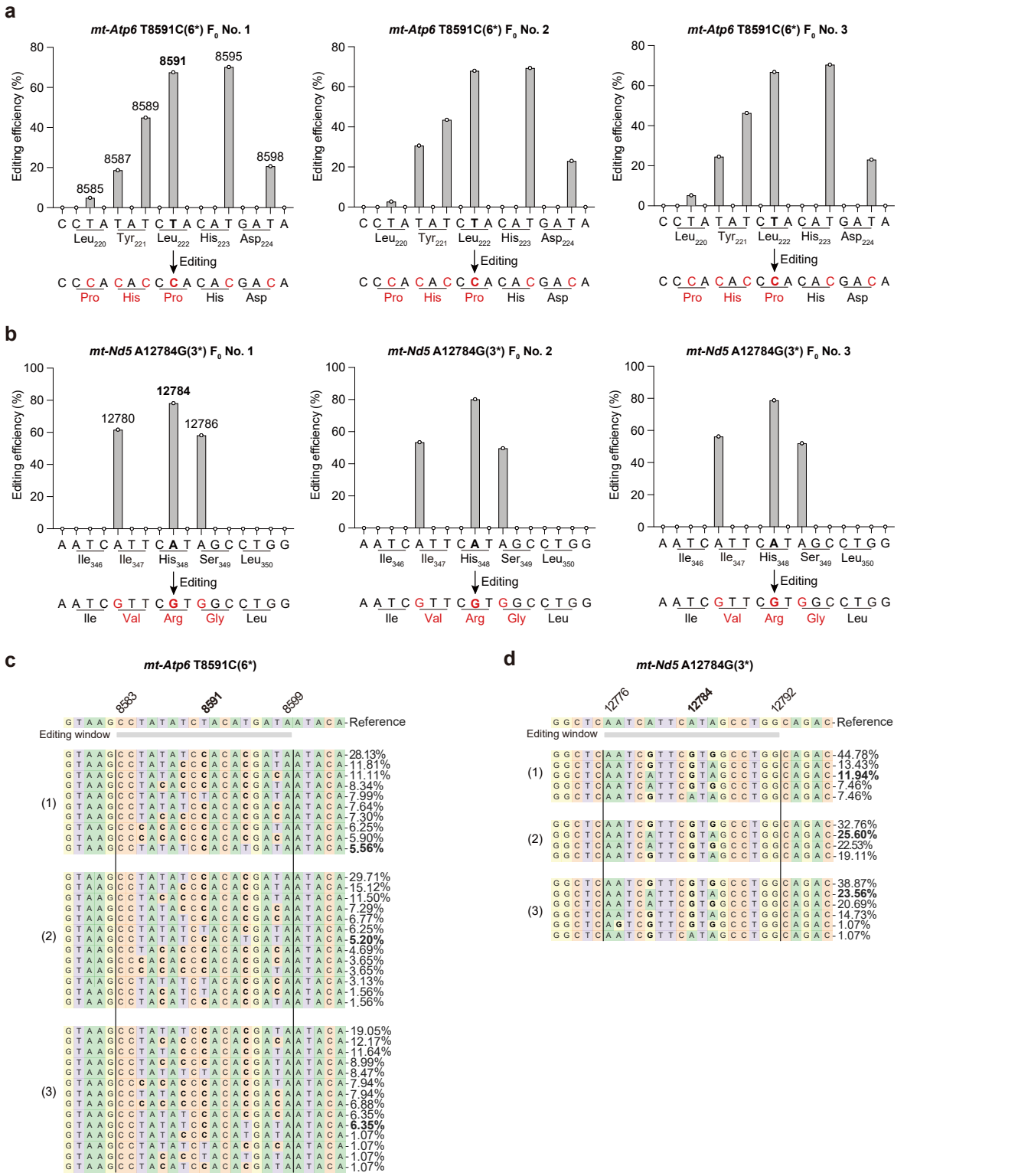

Extended Data Fig. 5 | Editing results of the target region in F_0 mice. a and **b**, Editing results within the editing window and corresponding amino acid changes in *mt-Atp6* T8591C(6*) F_0 mice (No. 1, 2, and 3) (**a**) and *mt-Nd5* A12784G(3*) F_0 mice (No. 1, 2, and 3) (**b**). **c**, Distribution of edited reads at the target region in three *mt-Atp6* T8591C(6*) F_0 mice. **d**, Distribution of edited reads at the target region in three *mt-Nd5* A12784G(3*) F_0 mice.

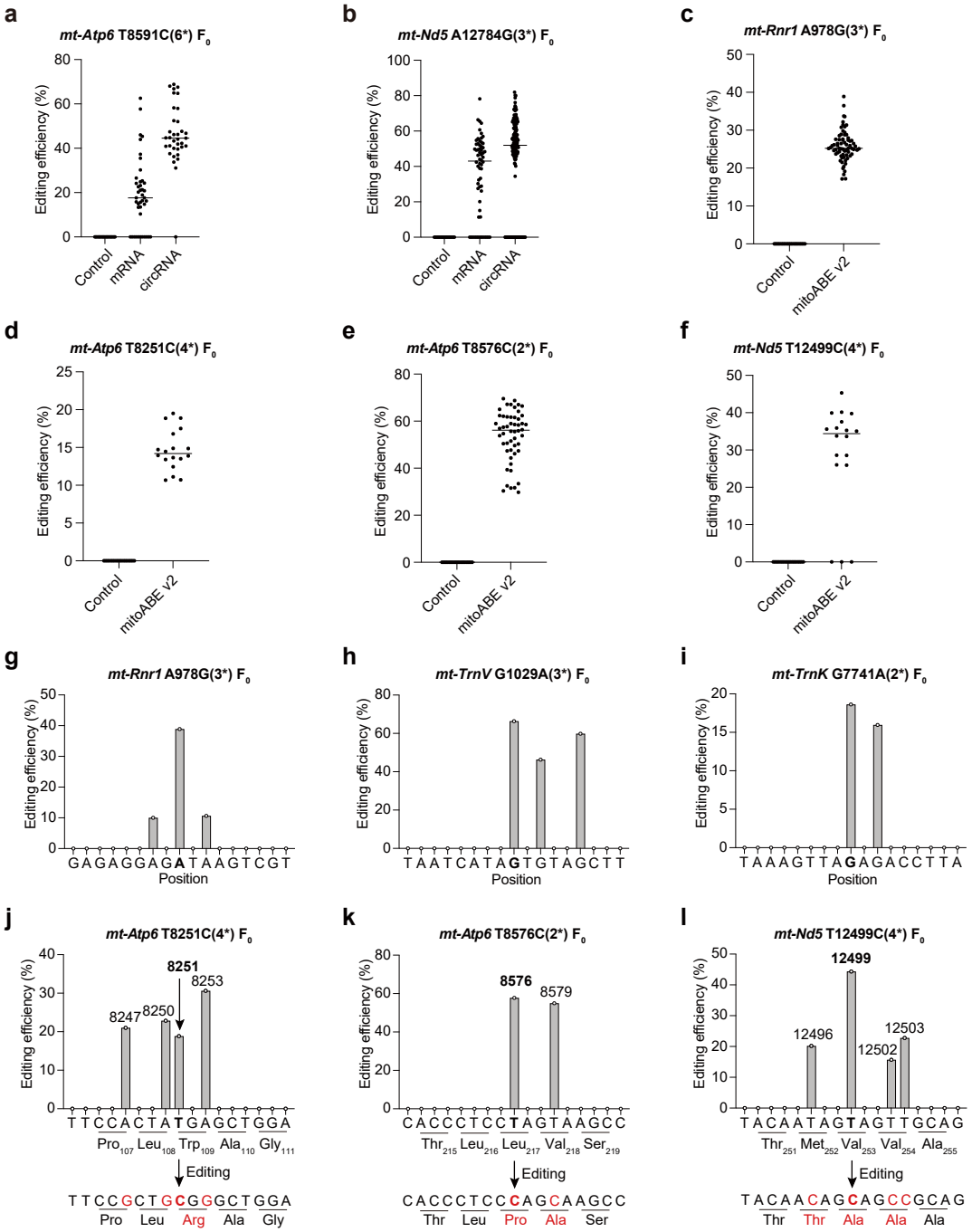

Extended Data Fig. 6 | Mitochondrial DNA target site editing efficiency of F_0 mice. a-b, Mitochondrial DNA target site editing efficiency of F_0 mice using mRNA- and circRNA-encoded mitoBEs v2 at *mt-Atp6* T8591C (**a**) and *mt-Nd5* A12784G (**b**). **c-f**, Mitochondrial DNA target site editing efficiency of F_0 mice at *mt-Rnr1* A978G (**c**), *mt-Atp6* T8251C (**d**), *mt-Atp6* T8576C (**e**), and *mt-Nd5* T12499C (**f**). For **a-f**, each dot represents the target site editing efficiency in one mouse. Number of F_0 mice n = 18, 42, 35 (**a**), 18, 62, 151 (**b**), 18, 70 (**c**), 18, 18 (**d**), 18, 52 (**e**), and 18, 18 (**f**); center lines: medians. **g-i**, Representative editing results within the editing window of *mt-Rnr1* A978G(3*) (**g**), *mt-TrnV* G1029A(3*) (**h**), and *mt-TrnK* G7741A(2*) (**i**) F_0 mice. **j-l**, Representative editing results within the editing window and corresponding amino acid changes of *mt-Atp6* T8251C(4*) (**j**), *mt-Atp6* T8576C(2*) (**k**), and *mt-Nd5* T12499C(4*) (**l**) F_0 mice. For **g-l**, the horizontal axis displays 17 bases within the editing window, with the bold base in the middle position indicating the target site. The vertical axis represents editing efficiency.

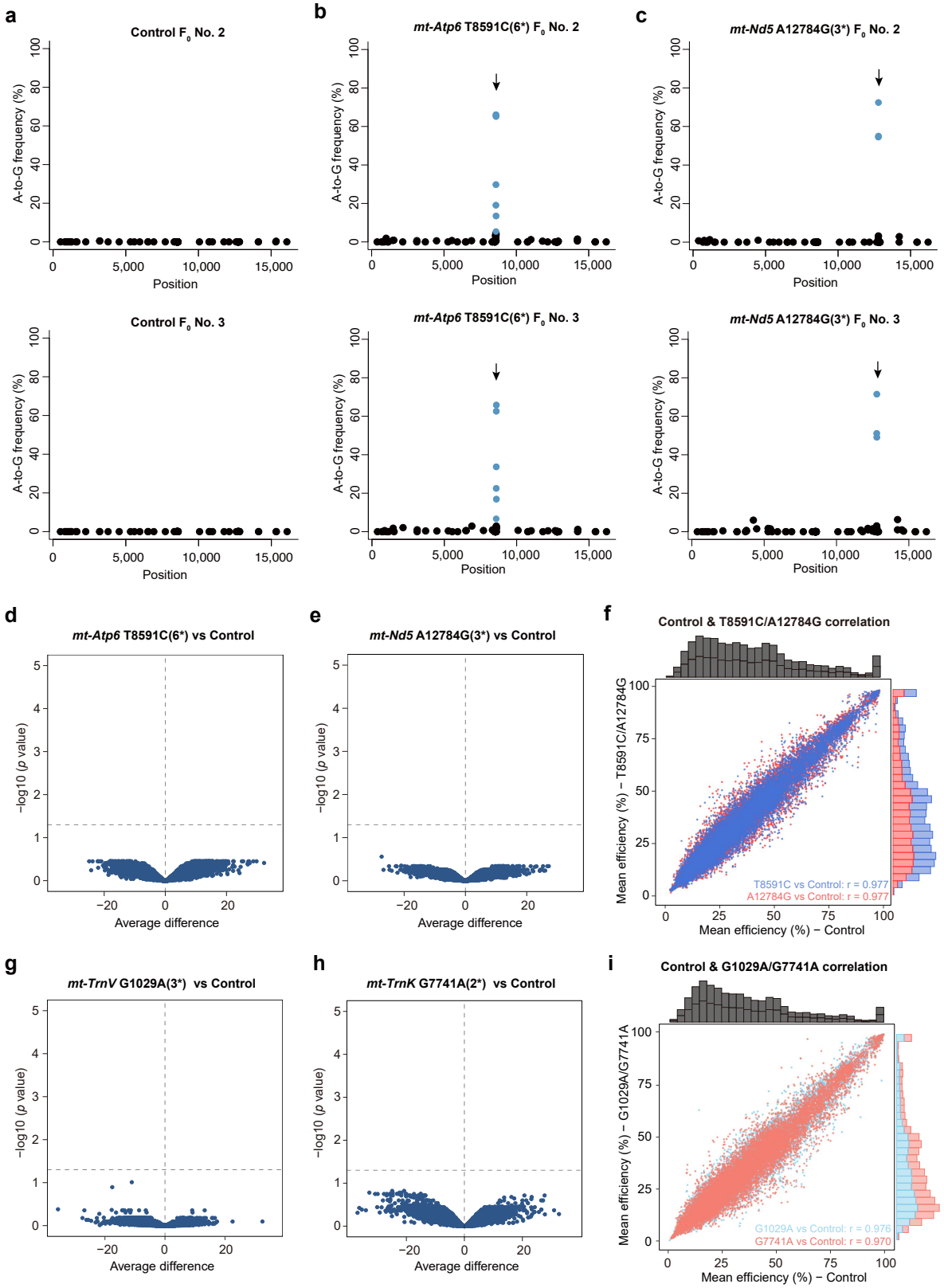

Extended Data Fig. 7 | See next page for caption.

Extended Data Fig. 7 | Off-target assessment on the whole genome of mouse models. a-c, The average A-to-G frequency on mitochondrial genome for control F_0 mice (No. 2 and 3) (**a**), *mt-Atp6* T8591C(6*) F_0 mice (No. 2 and 3) (**b**), and *mt-Nd5* A12784G(3*) F_0 mice (No. 2 and 3) (**c**). **d** and **e**, Volcano plots of differential site analysis between *mt-Atp6* T8591C(6*) (**d**), *mt-Nd5* A12784G(3*) (**e**) and control mice. **f**, Analysis of nuclear genome off-target effects of *mt-Atp6* T8591C(6*) and *mt-Nd5* A12784G(3*) mice using whole-genome sequencing. Pearson's correlation coefficient was used to assess the differential editing rate between *mt-Atp6* T8591C(6*) or *mt-Nd5* A12784G(3*) and control. **g** and **h**, Volcano plots of differential site analysis between *mt-TrnV* G1029A(3*) (**g**), *mt-TrnK* G7741A(2*) (**h**) and control mice. For **d**, **e**, **g** and **h**, the horizontal dashed line represents *p*-value = 0.05. The *p*-value is based on a two-tailed Student's t-test corrected for multiple comparisons, implemented using the R package limma. **i**, Analysis of nuclear genome off-target effects of *mt-TrnV* G1029A(3*) and *mt-TrnK* G7741A(2*) mice using whole-genome sequencing. Pearson's correlation coefficient was used to assess the differential editing rate between *mt-TrnV* G1029A(3*) or *mt-TrnK* G7741A(2*) and control. For **f** and **i**, Each point represents a SNP site. The horizontal axis shows average mutation rates. Marginal plots display rate distributions. For **d**-**i**, three independent experiments were performed.

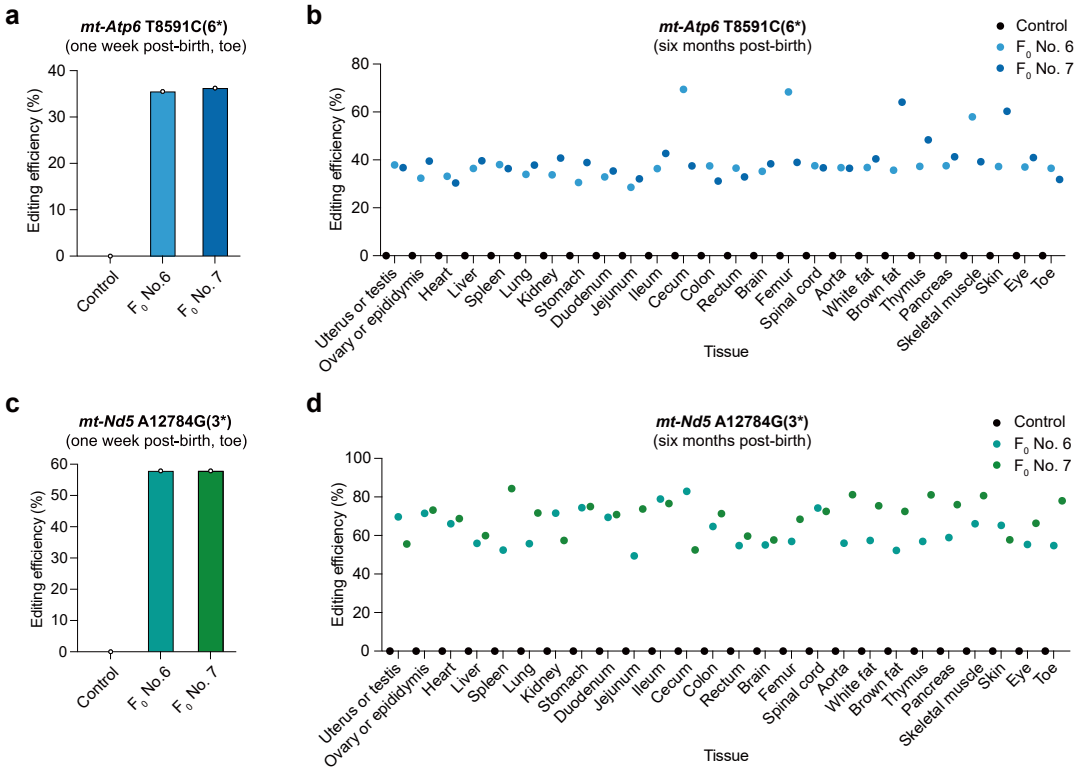

Extended Data Fig. 8 | Mitochondrial editing results are tissue-wide and durable. a, Mitochondrial DNA target site editing efficiency in toe tissue of control F_0 mouse and two *mt-Atp6* T8591C(6*) F_0 mice (No. 6 and 7) one week after birth. **b**, Mitochondrial DNA target site editing efficiency in 26 different tissues of control F_0 mouse and two *mt-Atp6* T8591C(6*) F_0 mice (No. 6 and 7) six months after birth. **c**, Mitochondrial DNA target site editing efficiency in toe tissue of control F_0 mouse and two *mt-Nd5* A12784G(3*) F_0 mice (No. 6 and 7) one week after birth. **d**, Mitochondrial DNA target site editing efficiency in 26 different tissues of control F_0 mouse and two *mt-Nd5* A12784G(3*) F_0 mice (No. 6 and 7) six months after birth.

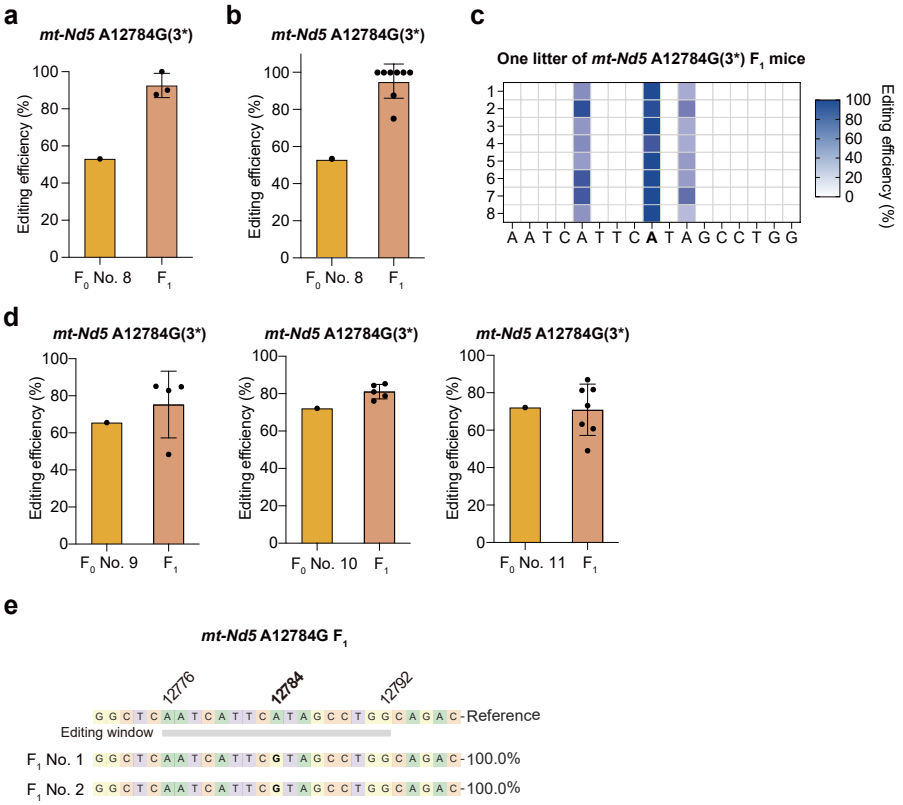

Extended Data Fig. 9 | *mt-Nd5* A12784G(3*) F_0 mice generate F_1 mice with 100% target site mutation load. a, Target site mutation load of the second litter of *mt-Nd5* A12784G(3*) F_1 mice born from *mt-Nd5* A12784G(3*) F_0 No. 8. **b**, Target site mutation load of the third litter of *mt-Nd5* A12784G(3*) F_1 mice born from *mt-Nd5* A12784G(3*) F_0 No. 8. **c**, Editing results within the editing window of the third litter of *mt-Nd5* A12784G(3*) F_1 mice born from *mt-Nd5* A12784G(3*) F_0 No. 8. The horizontal axis displays 17 bases within the editing window, with the bold base in the middle position indicating the target site 12784. **d**, Target site mutation load of F_1 mice generated from other three *mt-Nd5* A12784G(3*) F_0 mice. **e**, Distribution of edited reads at the target region in two *mt-Nd5* A12784G F_1 mice with only target site editing. For **a**, **b** and **d**, number of F_1 mice $n = 3$ (**a**), 8 (**b**), and 4, 5, 7 (**d**). Data are presented as mean ± s.d. from $n \geq 3$ independent biological replicates.

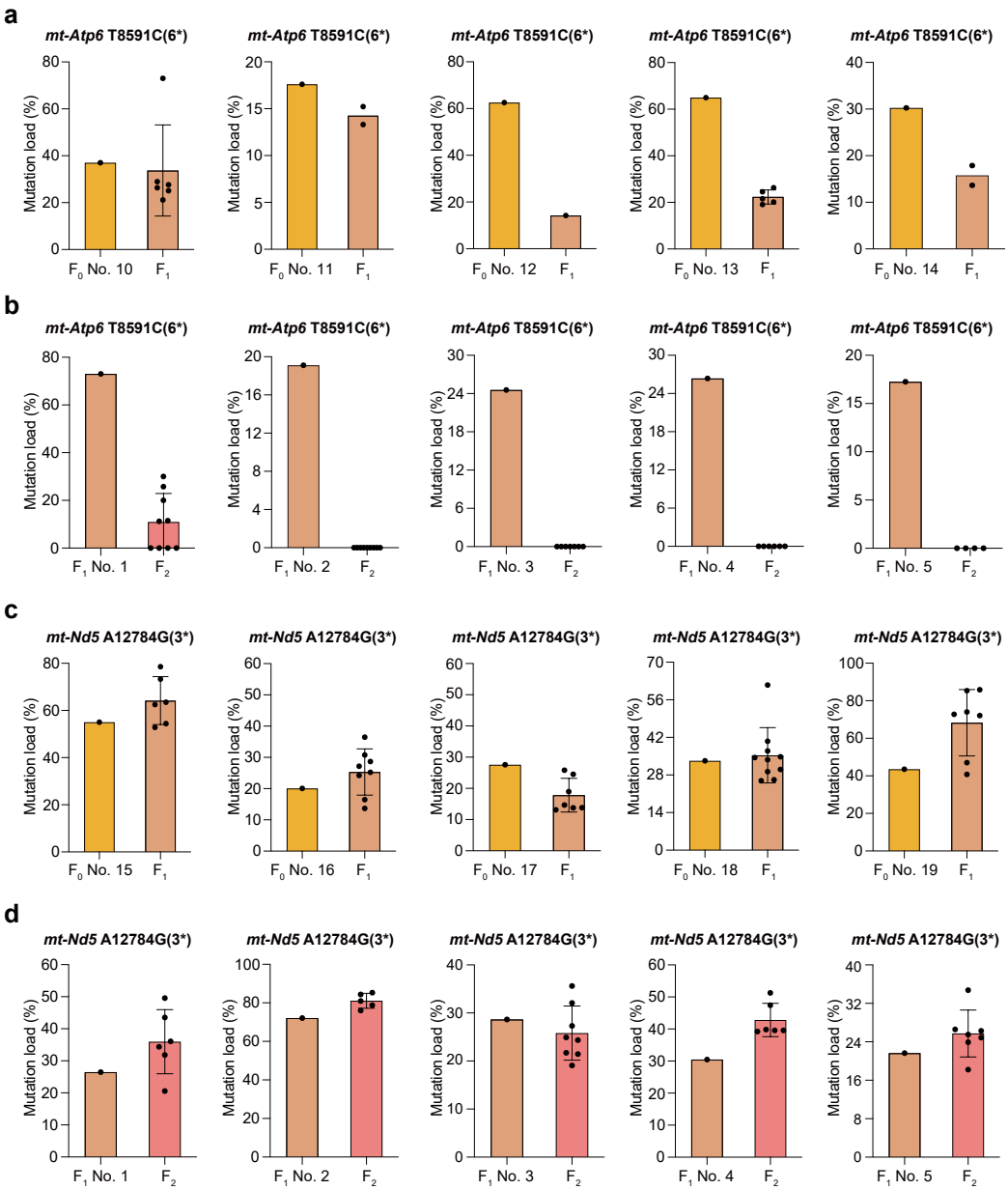

Extended Data Fig. 10 | The *mt-Atp6* T8591C mutation is rapidly lost during mouse passaging. a, Target site mutation load of F_1 generation mice derived from *mt-Atp6* T8591C(6*) F_0 mice. **b**, Target site mutation load of F_2 generation mice derived from *mt-Atp6* T8591C(6*) F_1 mice. **c**, Target site mutation load of F_1 generation mice derived from *mt-Nd5* A12784G(3*) F_0 mice. **d**, Target site mutation load of F_2 generation mice derived from *mt-Nd5* A12784G(3*) F_1 mice. For **a**-**d**, each dot represents the target site mutation load in one mouse. Number of F_1/F_2 mice n = 6, 2, 1, 5, 2 (**a**), 9, 9, 7, 6, 4 (**b**), 6, 8, 7, 10, 7 (**c**), and 6, 5, 8, 6, 7 (**d**). Data are presented as mean ± s.d. from $n > 3$ independent biological replicates.

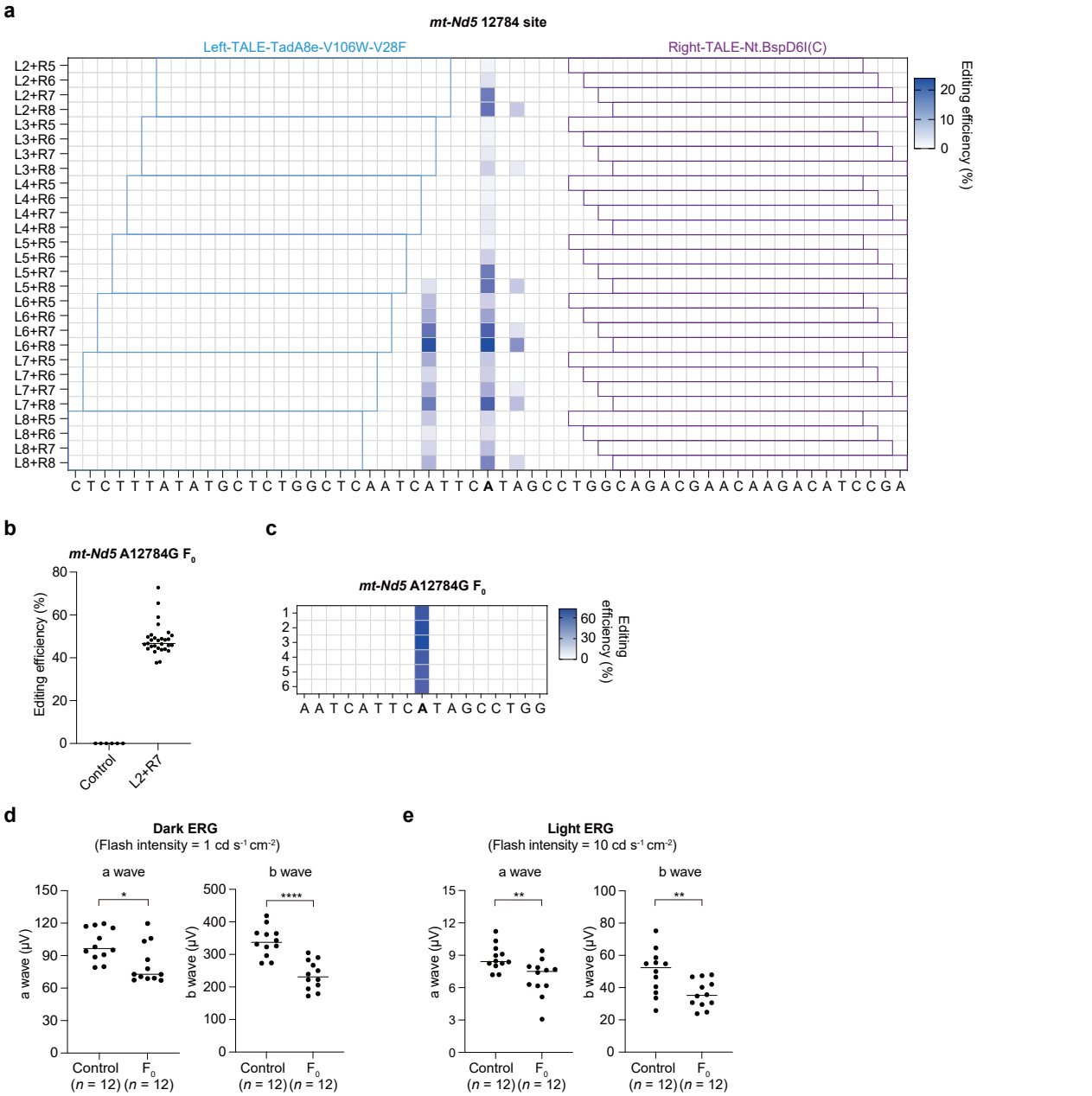

Extended Data Fig. 11 | The mouse model with *mt-Nd5* A12784G single base mutation exhibits LHON patient symptoms. a, Editing efficiency of different mitoBEs v2 pairs within the *mt-Nd5* 12784 site editing window in Neuro-2a cells. For example, the L2 + R5 pair indicates the left TALE recognition sequence is 2 bp away from the 12784 site, and the right TALE recognition sequence is 5 bp away. Data are presented as mean from $n = 3$ independent biological replicates. **b**, Mitochondrial DNA target site editing efficiency of F_0 mice using the L2 + R7 pair at *mt-Nd5* A12784G, with embryos injected only with buffer serving as controls. Number of mice $n = 6$ for control and 29 for L2 + R7; center lines: medians. **c**, Editing results within the window of *mt-Nd5* A12784G F_0 mice used for ERG. The horizontal axis shows 17 bases wider than the editing window, with the bold base indicating the target site 12784. **d**, Dark ERG under 1 cd s^{-1} cm^{-2} flash intensity condition of control mice and *mt-Nd5* A12784G F_0 mice. **e**, Light ERG under 10 cd s^{-1} cm^{-2} flash intensity condition of control mice and *mt-Nd5* A12784G F_0 mice. For **d** and **e**, 6 wild-type mice of the same age were used as controls. Number of eyes $n = 12$ for control and F_0; center lines: medians. The statistical test used was a two-tailed Student's t-test. The *p*-values are *0.0121 and ****<0.0001 for **d**, **0.0067 and **0.0089 for **e**.

nature portfolio

Corresponding author(s): Wensheng Wei, Zongyi Yi

Last updated by author(s): Oct 23, 2024

Reporting Summary

Nature Portfolio wishes to improve the reproducibility of the work that we publish. This form provides structure for consistency and transparency in reporting. For further information on Nature Portfolio policies, see our Editorial Policies and the Editorial Policy Checklist.

Statistics

For all statistical analyses, confirm that the following items are present in the figure legend, table legend, main text, or Methods section.

n/a	Confirmed	
☐	☒	The exact sample size (*n*) for each experimental group/condition, given as a discrete number and unit of measurement
☐	☒	A statement on whether measurements were taken from distinct samples or whether the same sample was measured repeatedly
☐	☒	The statistical test(s) used AND whether they are one- or two-sided *Only common tests should be described solely by name; describe more complex techniques in the Methods section.*
☒	☐	A description of all covariates tested
☒	☐	A description of any assumptions or corrections, such as tests of normality and adjustment for multiple comparisons
☐	☒	A full description of the statistical parameters including central tendency (e.g. means) or other basic estimates (e.g. regression coefficient) AND variation (e.g. standard deviation) or associated estimates of uncertainty (e.g. confidence intervals)
☐	☒	For null hypothesis testing, the test statistic (e.g. *F*, *t*, *r*) with confidence intervals, effect sizes, degrees of freedom and *P* value noted *Give P values as exact values whenever suitable.*
☒	☐	For Bayesian analysis, information on the choice of priors and Markov chain Monte Carlo settings
☒	☐	For hierarchical and complex designs, identification of the appropriate level for tests and full reporting of outcomes
☐	☒	Estimates of effect sizes (e.g. Cohen's *d*, Pearson's *r*), indicating how they were calculated

Our web collection on statistics for biologists contains articles on many of the points above.

Software and code

Policy information about availability of computer code

Data collection	labchart (heart rate), VEVO 770 (M-mode), Espion V6 (ERG)
Data analysis	BWA (v.0.7.10-r789), REDitools (v.1.0.4), and SAMtools (v1.1) are used for analysis of high-throughput sequencing data for targeted amplicon sequencing. FastQC (v0.12.1), fastp (0.23.2), bwa-mem2 (2.2.1), STAR (version 2.7.11a), GATK, GATK Mutect2, SAMtools (v1.1), and sambamba depth tool (version 0.6.6) were adopted for genome-wide DNA-sequencing and transcriptome-wide RNA-sequencing analysis. For TALE-dependent off-target analysis, we used the TALENoffer tool for prediction. The edited reads distribution in the targeted region was calculated by CRISPResso2. GraphPad Prism 8 was used for basic statistical analysis and graph production.

For manuscripts utilizing custom algorithms or software that are central to the research but not yet described in published literature, software must be made available to editors and reviewers. We strongly encourage code deposition in a community repository (e.g. GitHub). See the Nature Portfolio guidelines for submitting code & software for further information.

Data

Policy information about availability of data

All manuscripts must include a data availability statement. This statement should provide the following information, where applicable:

- Accession codes, unique identifiers, or web links for publicly available datasets
- A description of any restrictions on data availability
- For clinical datasets or third party data, please ensure that the statement adheres to our policy

Raw data from off-target analysis are available as a BioProject with project identifier PRJCA026376 in the China National Center for Bioinformation-National Genomics Data Center database. The confirmed human disease-related mitochondrial DNA mutations in Supplementary Table 4 are from the MITOMAP database. The human genome data GRCh38-hg38 and mouse genome data GRCm39-mm39 used in this study are from the Gencode database (accessible links: https://ftp.ebi.ac.uk/pub/databases/gencode).

Research involving human participants, their data, or biological material

Policy information about studies with human participants or human data. See also policy information about sex, gender (identity/presentation), and sexual orientation and race, ethnicity and racism.

Reporting on sex and gender	Not applicable.
Reporting on race, ethnicity, or other socially relevant groupings	Not applicable.
Population characteristics	Not applicable.
Recruitment	Not applicable.
Ethics oversight	Not applicable.

Note that full information on the approval of the study protocol must also be provided in the manuscript.

Field-specific reporting

Please select the one below that is the best fit for your research. If you are not sure, read the appropriate sections before making your selection.

☒ Life sciences ☐ Behavioural & social sciences ☐ Ecological, evolutionary & environmental sciences

For a reference copy of the document with all sections, see nature.com/documents/nr-reporting-summary-flat.pdf

Life sciences study design

All studies must disclose on these points even when the disclosure is negative.

Sample size	In this study, targeted base editing of cell lines and off-target analysis were done with three independent biological replicates performed in parallel. Three independent biological replicates met the needs of the unpaired two-tailed Student's T test, so we performed three or more independent replicates of each experiments. And the number of replicates was listed in the text and figure legends. For the detection of targeted site editing efficiency in F0 and F1 mouse tissues, we performed one test for each tissue of each mouse. For mouse experiments, typically, 6 mice meet the needs of experimental reproducibility, as we adopt a strategy of using 6 or more mice in experiments involving animals. These meet the requirements of the unpaired two-tailed Student's T test.
Data exclusions	No data were excluded.
Replication	The number of replications is always mentioned in text, methods and figure legends. All attempts at replication were successful.
Randomization	In this study, all samples were allocated into experimental groups randomly.
Blinding	For in vivo studies of phenotypes, all animals were numbered, wild-type and mtDNA mutant mice were mixed into cages, and experiments were conducted blinded. Cell line experiments do not need to be blinded because the samples come from the same source.

Reporting for specific materials, systems and methods

We require information from authors about some types of materials, experimental systems and methods used in many studies. Here, indicate whether each material, system or method listed is relevant to your study. If you are not sure if a list item applies to your research, read the appropriate section before selecting a response.

Materials & experimental systems

n/a	Involved in the study
☒	☐ Antibodies
☐	☒ Eukaryotic cell lines
☒	☐ Palaeontology and archaeology
☐	☒ Animals and other organisms
☒	☐ Clinical data
☒	☐ Dual use research of concern
☒	☐ Plants

Methods

n/a	Involved in the study
☒	☐ ChIP-seq
☒	☐ Flow cytometry
☒	☐ MRI-based neuroimaging

Eukaryotic cell lines

Policy information about cell lines and Sex and Gender in Research

Cell line source(s)	HEK293T (ATCC, CRL-3216) was from C. Zhang's laboratory (Peking University) and Neuro-2a (ATCC, CCL-131) cells was purchased from Pricella.
Authentication	STR analysis was used for cell line authentication.
Mycoplasma contamination	All cells tested negative for mycoplasma contamination.
Commonly misidentified lines (See ICLAC register)	No commonly misidentified cell lines were used.

Animals and other research organisms

Policy information about studies involving animals; ARRIVE guidelines recommended for reporting animal research, and Sex and Gender in Research

Laboratory animals	The mouse strain used in this article is C57BL/6J mouse strain. We performed genotyping on mice one week after birth, genotyping on different tissues on mice at 2 and 6 months of age, and phenotyping on mice at 2 months of age.
Wild animals	The study did not involve wild animals.
Reporting on sex	Sex was not considered in study design.
Field-collected samples	All mice were kept in the SPF animal room, with the temperature controlled at 22-24°C and relative humidity controlled at 30%-70% under a 12 hours dark-light cycle. No field collected samples were used in the study.
Ethics oversight	This study was approved by the Institutional Animal Care and Use Committee (IACUC) and the Animal Ethics Committee of Cyagen Biosciences. All mouse experiments were performed at Cyagen Biosciences (Project Number: TGBS230525JY3-S).

Note that full information on the approval of the study protocol must also be provided in the manuscript.

Plants

Seed stocks	Plants were not involved in the study.
Novel plant genotypes	Plants were not involved in the study.
Authentication	Plants were not involved in the study.